Journal Pre-proof

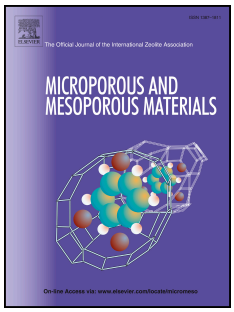

Local environment and catalytic property of External Lewis acid sites in hierarchical lamellar titanium Silicalite-1 zeolites

Wei Wu, Dat T. Tran, Sichao Cheng, Yuan Zhang, Na Li, Huiyong Chen, Ya-Huei (Cathy) Chin, Libo Yao, Dongxia Liu

PII: S1387-1811(20)30710-1

DOI: https://doi.org/10.1016/j.micromeso.2020.110710

Reference: MICMAT 110710

To appear in: *Microporous and Mesoporous Materials*

Received Date: 23 August 2020

Revised Date: 15 October 2020

Accepted Date: 16 October 2020

Please cite this article as: W. Wu, D.T. Tran, S. Cheng, Y. Zhang, N. Li, H. Chen, Y.-H.(C.) Chin, L. Yao, D. Liu, Local environment and catalytic property of External Lewis acid sites in hierarchical lamellar titanium Silicalite-1 zeolites, *Microporous and Mesoporous Materials* (2020), doi: https://doi.org/10.1016/j.micromeso.2020.110710.

Author contributions:

Wei Wu did the catalyst synthesis, majority of catalyst characterizations, and catalysis testing. Dat T. Tran collected data on the DR UV-vis characterization of TS-1 zeolites. Sichao Cheng and Yuan Zhang measured acidity of the catalyst materials. Na Li and Huiyong Chen carried out the elemental composition analysis of zeolites. Ya-Huei (Cathy) Chin and Libo Yao measured FTIR spectra of the catalyst samples. Dongxia Liu supervised the project. Wei Wu, Ya-Huei (Cathy) Chin and Dongxia Liu did data discussion and contributed to the manuscript writing.

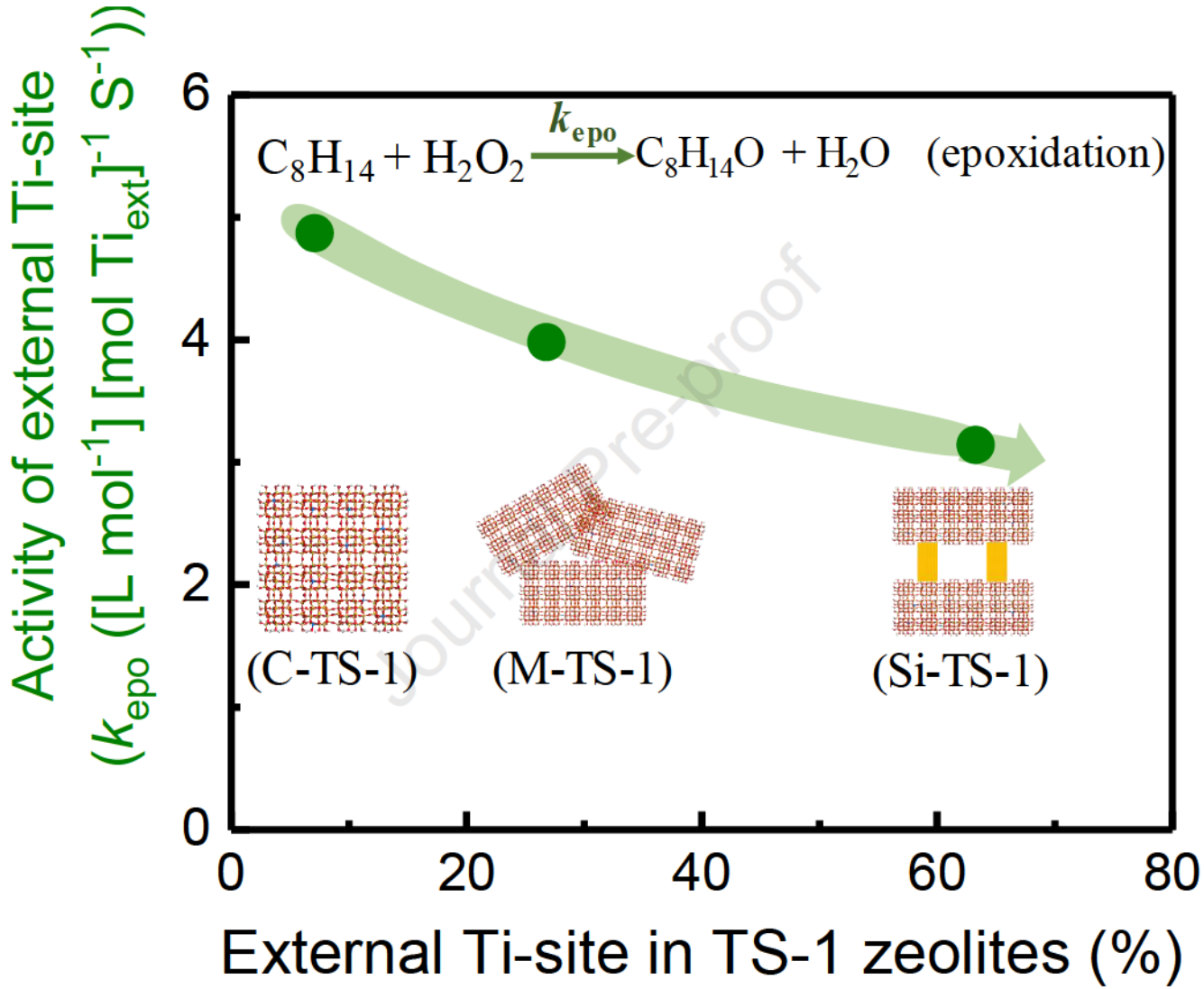

Local Environment and Catalytic Property of External Lewis Acid Sites in Hierarchical Lamellar Titanium Silicalite-1 Zeolites

Wei Wu[†], Dat T. Tran[‡], Sichao Cheng[†], Yuan Zhang[†], Na Li[§], Huiyong Chen[§], Ya-Huei (Cathy) Chin[ǀ], Libo Yao[⊥] and Dongxia Liu[†*]

[†]Department of Chemical and Biomolecular Engineering, University of Maryland, College Park, MD 20742, USA

[‡] CCDC Army Research Laboratory, FCDD-RLS-DE, 2800 Powder Mill Road, Adelphi, MD 20783, USA

[§]School of Chemical Engineering, Northwest University, Xi'an, Shaanxi, 710069, China

[ǀ]Department of Chemical Engineering and Applied Chemistry, University of Toronto, 200 College Street, Toronto, ON, M5S 3E5, Canada

[⊥] Department of Chemical and Biomolecular Engineering, University of Akron, Akron, OH, 44325, USA

*Corresponding author:
Prof. Dongxia Liu
Email: liud@umd.edu
Phone: (+1) 301-405-3522
Fax: (+1) 301-405-0523

Abstract: Hierarchical two-dimensional (2D) lamellar zeolites represent a young emerging field and a novel expression of the zeolite frameworks. Accompanied with synthesis and catalytic performance investigation, assessment on the local environment and catalytic behavior of acid sites in 2D zeolites are needed. Here, we described the local environment of Lewis acid sites and evaluated catalytic activities of external acid sites (i.e. sites on external surface and in mesopores) in 2D lamellar titanium silicalite-1 (TS-1) zeolites. For comparison purpose, four TS-1 zeolites, including 3D TS-1, multilamellar 2D TS-1 without pillarization and with pillarization by silica and silica/titania, respectively, were prepared. The local environment of Ti-sites, including coordination status of Ti-atom, speciation of hydroxyl (-OH) group that hints degree of confinement, acid site strength and accessibility, was collectively assessed by spectroscopic and organic base titration measurements. Kinetic studies of cyclooctene (C_8H_{14}) epoxidation with hydrogen peroxide (H_2O_2) discerned catalytic activity of external Ti-sites that decreased with increasing mesoporosity due to decrease in site confinement.

Keywords: 2-dimensional zeolite, titanium silicalite-1, hierarchical zeolite, Lewis acidity, cyclooctene epoxidation.

1. Introduction

Since the first disclosure of titanium silicalite-1 (TS-1) zeolite from Enichem in 1983,[1] tremendous efforts have been devoted to study its Lewis acidity from titanium (Ti) centers and catalytic performance in oxidation reactions. Lewis acid catalyzed phenol hydroxylation,[2-4] cyclohexanone ammoximation[5-8] and propylene epoxidation[9-11] have been practiced at the industrial scale. The TS-1 catalyst is also studied for benzene hydroxylation,[12, 13] linear/cyclic olefins epoxidation,[14-19] terpenes epoxidation[17, 20] and allyl alcohol/chloride epoxidation[21-23] reactions. TS-1 zeolites, however, exhibit poor catalytic performance for the conversion of bulky reactants, when the kinetic diameters of these reactants are larger than the zeolite micropores (10-membered ring (10MR), 0.51×0.55 nm along *a*-axis and 0.53×0.56 nm along *b*-axis) and, as a result, their transport to the Ti-active centers during catalysis are severely restricted. In order to overcome this constraint, attempts to alter the transport properties through synthetic strategies such as synthesizing Ti-containing zeolites with extra-large (i.e. 12MR and 14MR) micropore apertures[24-27] or hierarchical TS-1 zeolite architectures[18-20] have been explored.

Hierarchical zeolites, consisting of dual meso-/micropores, have shown remarkable catalytic performance for reactions involving bulky molecules in the past decades.[28] Among the hierarchical zeolites, two-dimensional (2D) zeolite nanosheet and its assembly structures are unique. The assembly increases the external surface area by introducing interlayer mesopores. Such structures markedly increase the accessibility of reactant to the active sites and at the same time retain the microporosity within zeolitic

layers, often required for catalysis. The synthesis of TS-1 nanosheet structures, including unilamellar[18], multilamellar[19, 20, 29] and pillared[20, 29] architectures, have been reported recently. In these TS-1 nanosheet materials, the Ti-centers are positioned tetrahedrally in zeolite framework (similar to that of 3D microporous TS-1 zeolite), which are realized by isomorphic substitution of silicon element during hydrothermal crystallization.[30] The high external surface area of TS-1 zeolite nanosheet architectures enables the post-synthetic method to introduce Ti-active sites. For example, the unilamellar TS-1 nanosheet was grafted with Ti-active centres from the titanium(IV) butoxide precursor on its external surface[17]. Similarly, the delaminated siliceous MWW-type zeolites, ITQ-2[31, 32] and UCB-4[33], were grafted with Ti-sites from the titanocene and calix[4]arene-Ti^{IV} precursors. These post-synthetic methods created Ti-sites with increased accessibility to bulky molecules. The pillarization treatment of multilamellar TS-1 nanosheets can also introduce additional Ti-active sites besides those inherently present in the framework. For instance, the intercalation of pillaring precursors by dispersing 2D zeolite in an alkoxide liquid (a mixture of tetrabutoxytitanium (TBOT) and tetraethyl orthosilicate (TEOS)) and hydrolyzing entrapped alkoxide formed the silica/titania (SiO_2/TiO_2) pillars in pillared MWW or TS-1 zeolite. These pillared zeolites showed improvement in converting bulky reactants in epoxidation reactions, when comparing to their non-pillared counterparts.[20, 29, 34, 35]

Besides the above studies on the synthesis and catalytic activity of 2D TS-1 zeolites, quantitative assessment on the local environment and catalytic behavior of Lewis acidic Ti-centers is also needed. Comparing to those established for Brønsted acidity[36-39] in 2D zeolites, quantification of Lewis acidity, local Lewis acid site

environment and reactivity in catalytic reactions are limited. A recent work by Shamzhy etc. quantified the Lewis acidity, acid strength and accessibility of 2D TS-1 zeolites using the Fourier-transform infrared (FTIR) studies of adsorbed organic bases[40]. Here, we made an effort to characterize the acid site local environment including coordination status of Ti-atom, speciation of hydroxyl (-OH) group that hints for the degree of acid site confinement, site strength and accessibility to bulky molecules of Lewis acidic Ti-sites, in hierarchical 2D TS-1 zeolites that include multilamellar TS-1 (M-TS-1), SiO_2-pillared TS-1 (Si-TS-1) and SiO_2/TiO_2-pillared TS-1 (Si/Ti-TS-1). The combination of spectroscopic measurement, organic base titration and in-situ poisoning of catalytic epoxidation of cyclooctene (C_8H_{14}) with hydrogen peroxide (H_2O_2) was used for this purpose.

In addition, the catalytic activity of external acid sites in these 2D TS-1 zeolites were investigated by running C_8H_{14}-H_2O_2 reactions in the absence of poisoning molecules. The kinetics of C_8H_{14} conversion can probe exclusively the catalytic activity of Ti-centers on external surface and in mesopores (i.e. external Ti-sites, herein denoted as Ti_{ext}) because C_8H_{14} is too bulky (kinetic diameter of 0.77 nm)[29, 41] to access to those enclosed within the 10 MR micropores. In contrast, H_2O_2 consumption occurs via the catalytic epoxidation with C_8H_{14} and undesired, non-productive catalytic decomposition by Ti-sites and non-productive thermal decomposition, the latter occurs even without a catalyst. Kinetic decoupling of these three concomitant H_2O_2 conversion pathways is conducted to enable the assessment on the catalytic behavior of Ti_{ext}-sites. The present study will guide in-depth understanding of Lewis acidity in 2D zeolite materials.

2. Experimental

2.1. Materials

Tetrabutoxytitanium (TBOT, 99% purity), sodium hydroxide (NaOH, 97.0% purity), 1-butanol (BuOH, 99% purity), tetra-n-propylammonium hydroxide (TPAOH, 40wt% solution) and methylphosphonic acid (MPA, 98% purity), sulfuric acid (H_2SO_4, 95% purity), pyridine (ultrapure, 99.5% purity) and potassium titanium (IV) oxalate ($K_2C_4O_9Ti \cdot 2H_2O$, 98% purity) were supplied by Alfa Aesar. Tetraethyl orthosilicate (TEOS, 98% purity) and hexanediamine ($C_6H_{16}N_2$, 98% purity) were purchased from Sigma-Aldrich. Cyclooctene (95% purity) was purchased from TCI. Hydrogen peroxide (H_2O_2, 30 wt% solution) was purchased from EMD Millipore Corporation. Ethanol (200 proof) was purchased from Pharmco. Deionized (DI) water was used throughout the experiments. Diquaternary ammonium surfactant ($[C_{22}H_{45}\text{-}N^+(CH_3)_2\text{-}C_6H_{12}\text{-}N^+(CH_3)_2\text{-}C_6H_{13}]Br_2^-$, ($C_{22\text{-}6\text{-}6}$)) was synthesized following previously reported method,[28] and the synthesis procedure has also been described in detail in our previous publications.[29, 38, 42]

2.2. Synthesis of TS-1 zeolites

The multilamellar TS-1 was used as the precursor of hierarchical lamellar TS-1 zeolites (designated as M-TS-1(P)). It was synthesized using the method reported in our previous work.[29] In the synthesis, 2.02 g of hexanediamine was dissolved in 20 cm^3 of DI water, followed by adding 6.16 g TEOS. The resultant mixture was magnetically stirred at room temperature until a homogeneous solution was formed. Then, the mixture

was cooled in an iced bath, and a freshly prepared solution of 0.10 g TBOT in 0.64 g 1-butanol (BuOH) was added dropwise under vigorous stirring. The mixture was then heated to 333 K and added with $C_{22\text{-}6\text{-}6}$ solution that was prepared by dissolving 1.48 g $C_{22\text{-}6\text{-}6}$ in 10.8 g water. The resultant zeolite synthesis gel was aged at 333 K for 3 h under stirring. The molar composition of the zeolite synthetic gel mixture was $100SiO_2/7C_{22\text{-}6\text{-}6}/1TiO_2/6000H_2O/30BuOH/60C_6H_{16}N_2$. Lastly, the synthetic gel was transferred into a Teflon-lined autoclave and crystallization of zeolite was conducted at 413 K for 10 days under tumbling condition (30 rpm speed). After crystallization, the zeolite sample was centrifuged, washed with DI water, and dried at 343 K overnight. One portion of M-TS-1(P) was calcined at 823 K for 4 h under air atmosphere to produce M-TS-1 zeolite. The other portion of M-TS-1(P) was processed with following methods to form pillared TS-1 zeolites.

The silica pillared TS-1 nanosheet (defined as Si-TS-1) was prepared by dispersing the M-TS-1(P) precursor in a TEOS solvent at a M-TS-1(P)-to-TEOS solvent weight ratio of 5. The resultant suspension was sealed in a flask equipped with a septum under the N_2 atmosphere and kept at 351 K in an oil bath for 24 h. The zeolite sample was collected by filtration and dried under ambient condition. Hydrolysis of the as-obtained zeolite sample was carried out by dispersing in an aqueous basic NaOH solution with pH of 8 at a NaOH solution to solid zeolite weight ratio of 10. After stirring the mixture at 333 K for 24h, the sample was collected by centrifugation, washed with DI water twice, and then dried under ambient condition. Finally, the sample was calcined at 723 K for 6 h under N_2 atmosphere and 823 K for 12 h under air atmosphere. The SiO_2/TiO_2 pillared TS-1 (abbreviated as Si/Ti-TS-1) zeolite was prepared using the same

method as that of Si-TS-1, except that the TEOS solvent was replaced by TEOS/TBOT mixture. The molar ratio of TEOS/TBOT was controlled at 100.

The conventional microporous TS-1 (named as C-TS-1) zeolite was used as a control sample and synthesized following previously established protocol, as described in detail elsewhere.[29] The molar composition of the C-TS-1 zeolite precursor was $100SiO_2/15TPAOH/1TiO_2/1500H_2O$. Typically, 10.00 g TEOS was mixed with 3.59 g TPAOH (40wt% purity) and 10.54 g DI water. After stirring for 1 h, 0.16 g TBOT in 0.74 g isopropanol solution was added dropwise into the solution. The mixture was heated to 353 K under stirring to remove isopropanol. The obtained zeolite synthesis gel was transferred into a Teflon-lined autoclave and placed in a convective oven at 443 K for 72 h under static condition. After crystallization, the zeolite sample was centrifuged, washed with DI water, and dried at 343 K overnight. Finally, the zeolite was calcined using the same procedure as M-TS-1 zeolite.

All the TS-1 samples, including C-TS-1, M-TS-1, Si-TS-1 and Si/Ti-TS-1, were ion-exchanged three times using 1 M aqueous NH_4NO_3 (weight ratio of zeolite to NH_4NO_3 solution = 1:10) at 353 K for 4 h, and subsequently, centrifuged, washed with DI water, and dried at 343 K overnight. All samples were then treated in dry air (1.67 cm^3 s^{-1}) by increasing the temperature from ambient to 823 K at 0.167 K s^{-1} and holding for 4 h, prior to the characterization and catalytic tests. Figure 1 shows the schematic structures of hierarchical 2D lamellar M-TS-1, Si-TS-1 and Si/Ti-TS-1 zeolites, together with 3D TS-1 for comparison.

2.3. Materials characterization

Powder X-Ray diffraction (XRD) patterns were recorded using a Bruker D8 Advance Lynx Powder Diffractometer (LynxEye PSD detector, sealed tube, Cu Kα radiation with Ni β-filter). Scanning electron microscopy (SEM) images were taken on a Hitachi SU-70 electron microscope to visualize the zeolite morphologies. Transmission electron microscopy (TEM) images were obtained on a JEM 2100 LaB6 electron microscope. N_2 adsorption-desorption isotherms of the samples were measured using an Autosorb-iQ analyzer (Quantachrome Instruments) at 77 K. The samples were outgassed at 573 K for 8 h at 1 mm Hg pressure prior to measurements. Si and Ti contents of the zeolite samples were determined by inductively coupled plasma optical emission spectroscopy (ICP-OES, Perkin Elmer Optima 7000). Diffuse reflectance (DR) Ultraviolet-Visible (UV-Vis) spectra were obtained using an Ocean Optics USB2000+ spectrometer equipped with an IS200-4 integrating sphere detector, and the white high reflectance sphere material (manufactured from Polytetrafluoroethylene (PTFE) based bulk material) was used as the reference. Fourier transform infrared (FTIR) spectra of zeolite samples were recorded using a spectrometer (Nicolet Magna-IR 560) with a resolution of 2 cm^{-1}.

2.4. Acidity determination in TS-1 zeolites

The types of acidity in hierarchical lamellar TS-1 and C-TS-1 zeolite samples were identified by Fourier transform infrared (FTIR, Bruker Vertex 70) of adsorbed pyridine. The measurement was carried out on self-supported zeolite wafers (10 mg cm^{-2}) of original samples previously activated at 673 K and 102 Pa for 2 h. After wafer activation, the background spectrum was recorded, and then pyridine (650 Pa) was introduced into the vacuum IR cell and adsorbed onto the zeolite at 423 K. Desorption of

physisorbed pyridine was performed by heating under vacuum for over 1 h period, followed by an IR measurement at room temperature.

To quantify the acid site concentrations in TS-1 zeolites, chemical titration using pyridine titrant was carried out in a tubular packed-bed quartz reactor (10 mm inner diameter) under atmospheric pressure. A resistively heated furnace (National Electric Furnace FA120 type) was used to heat the reactor to desired temperatures. In the experiment, the catalyst sample (0.100 g) was supported on a coarse quartz disk inside the reactor and was treated in N_2 (0.5 cm^3 s^{-1}, ultrapure, Airgas) at 773 K (ramp rate of 0.0167 K s^{-1}) for 3 h prior to cooling to the titration temperature. Titration studies were carried out at two temperatures, 423 and 373 K. Liquid pyridine (0.5 g) and ethanol (15.0 g) were mixed and then introduced continuously into a heated vaporizer, kept above 383 K, using a syringe pump (Cole Parmer 74900 series). In the vaporizer, the mixture was evaporated and mixed with the Ar flow stream to generate a vapor pyridine/ethanol/Ar feed stream (4.97×10^{-9} mol s^{-1} pyridine, 2.37×10^{-6} mol s^{-1} ethanol and 0.8 cm^3 s^{-1} Ar (99.99% purity, Airgas)), which was introduced continuously into the catalyst. All gas transfer lines were heated above 383 K to prevent condensation of pyridine/ethanol. Pyridine adsorption was recorded by measuring the effluent using a gas chromatograph (Agilent 6890 GC) equipped with DB-WAX column connected to a flame ionization detector. After adsorption saturation, the injection of pyridine/ethanol mixture was stopped, and the physisorbed pyridine was continuously removed by purging with Ar (0.8 cm^3 s^{-1}) for 3 h. The concentrations of acid sites were calculated from the pyridine adsorption and desorption curves, assuming that each Ti center binds to a pyridine molecule (pyridine/Ti ratio = 1)[38, 43].

2.5. Catalytic cyclooctene epoxidation reaction

2.5.1 Cyclooctene epoxidation in the absence of organic titrant

The liquid phase cyclooctene epoxidation with H_2O_2 was carried out in an isothermal batch reactor made of thick-walled glass sealed with crimp tops (20 cm^3, PTFE/silicone septum). The reactor was placed inside the hole of a copper cylinder shape incense holder that was heated on a stirring hot plate. The reaction was run at autogenous pressure under constant magnetic stirring (0.5-inch stirring bar, 500 rpm stirring speed). During the experiment, the glass reactor was charged with 0.050 g catalyst, 0.526 g cyclooctene, 6.288 g acetonitrile and 0.255 g H_2O_2 (30 wt% aqueous solution) in sequence. After sealing the reactor, it was placed into the copper cylinder shape incense holder that was pre-heated at 333 K and kept for the desired reaction time. Afterwards, the reaction was terminated by quenching the reactor in an ice bath. The influence of external mass transfer limitations on the reaction was ruled out by running the reaction at a high stirring speed, showing a further increase in the stirring speed did not enhance the reaction rate anymore.

Three concomitant reaction pathways occur during C_8H_{14}-H_2O_2 reactions to consume H_2O_2 reactant, as depicted in Figure 2. This includes (i) C_8H_{14} epoxidation (Pathway 1), which is catalyzed exclusively by external Ti_{ext} sites, because C_8H_{14} cannot gain access to the Ti sites inside the micropores, (ii) catalytic H_2O_2 decomposition (Pathway 2), occurred at all Ti sites (i.e. Ti_{total}), because unlike C_8H_{14}, H_2O_2 has a small kinetic diameter of 0.28 nm[44, 45] and thus can travel into micropores to access both external and internal active Ti-sites, and (iii) non-catalytic thermal decomposition (Pathway 3), which occurs homogeneously, even without the presence of a catalyst. To

study the pathways for H_2O_2 decomposition, two control experiments were conducted in the similar reaction conditions to that of C_8H_{14} epoxidation. In the first control experiment, the reaction was carried out as described above without any catalyst. This test is used to examine the non-catalytic thermal decomposition of H_2O_2 in the reaction. In the second control experiment, the C_8H_{14} reactant was not used, but other conditions remained the same. The rates obtained from these control experiments, together with that of H_2O_2 consumption in epoxidation of C_8H_{14}, allow us to decouple all H_2O_2 reaction pathways and discern their individual rates.

The conversion of cyclooctene reactant was traced by analyzing the cyclooctene concentration with a gas chromatograph (Agilent 7890A) equipped with a methylsiloxane capillary column (HP-1, 50.0 m × 320 μm × 0.52 μm) connected to a flame ionization detector (FID). The conversion of H_2O_2 in the reaction was tracked via a spectrophotometric method[46] on a HP 8453 UV-visible spectrophotometer. The UV-absorption centered at 398 nm in the spectra can be ascribed to the titanium (IV) - peroxide complex formed from the reaction between H_2O_2 and potassium titanium (IV) oxalate stock solution. The stock solution was prepared by adding 27.2 cm^3 sulfuric acid (95% purity, Alfa Aesar) and 3.54 g potassium titanium (IV) oxalate (98% purity, Alfa Aesar) into 30 cm^3 DI water. Afterwards, additional DI water was added such that the total volume of the stock solution equaled 100 cm^3. For the analysis of each sample, 0.040 g reaction mixture was mixed with 20 cm^3 DI water and 0.500 g potassium titanium (IV) oxalate stock solution to form the titanium (IV) - peroxide complex and the complex solution was analyzed using the UV-visible spectrophotometer to obtain the H_2O_2 concentration.

2.5.2 Cyclooctene epoxidation in the presence of methylphosphonic acid organic titrant

To probe the accessibility of active sites in hierarchical lamellar TS-1 samples, the acid site titration by methylphosphonic acid (MPA) molecules in the cyclooctene epoxidation reaction was conducted. The experimental set-up and reaction conditions were the same as those described in Section 2.5.1 except that, in this series of experiments, MPA was added. In an experiment, the zeolite catalyst, desired amount of MPA, DI water and cyclooctene were first added into the reactor in sequence, and then the resultant mixture was stirred at room temperature for 3 h before H_2O_2 addition. The 3 h mixing prior to H_2O_2 addition ensured MPA molecules to be adsorbed onto all accessible active sites of TS-1 zeolites. The reaction mixture was sampled at the reaction time of 2 h to obtain the rate in presence of MPA molecules in C_8H_{14}- H_2O_2 reaction. The rate was then divided by the rate that was measured in the absence of any MPA molecules to calculate for a normalized rate. A series of experiments with different MPA concentrations, which correspond to different MPA/Ti ratios, were conducted on each TS-1 zeolite. The extrapolation of the normalized rate to zero in the plot of normalized rate versus MPA/Ti ratio is the accessibility of Ti-sites to bulky MPA molecules in the C_8H_{14}- H_2O_2 reaction.

3. Results and discussion

3.1. Structural and textural properties

Figure 3 presents the XRD patterns of the conventional 3D C-TS-1 and 2D hierarchical M-TS-1, Si/Ti-TS-1 and Si-TS-1 zeolites. The wide-angle XRD peaks of

these materials are nearly the same with the characteristics of a crystalline MFI zeolite structure.[18, 28] In the low-angle range, the diffraction peaks show the long-range ordering of 2D nanosheets in the pillared TS-1 samples (i.e. Si/Ti-TS-1 and Si-TS-1), consistent with the structure schemes shown in Figure 1. Comparing the peak intensity of Si/Ti-TS-1 to that of the Si-TS-1sample, Si/Ti-TS-1 exhibited a lower peak intensity, suggesting partial loss of the long-range ordering in TS-1 nanosheets upon pillarization with the TBOT/TEOS mixture. The C-TS-1 and M-TS-1 do not have any nanosheet ordering structure, as indicated by the absence of low-angle XRD peaks.

The morphology of all the TS-1 zeolites was examined by SEM and TEM, and the representative micrographs are shown in Figure 4. The 3D C-TS-1 has short cylinder-like particles with an average width of ~250 nm, a thickness of ~200 nm and well-crystallized smooth surfaces (Figure 4a). The lattice fringe can be clearly seen in the TEM image (Figure 4e). The M-TS-1 (Figure 4b and 4f) sample has a plate-like morphology. Each plate contains a few TS-1 nanosheet layers, and interlayer distance is close to 1.2 nm. Both Si-TS-1 (Figure 4c and 4g) and Si/Ti-TS-1 (Figure 4d and 4h) samples have similar plate-like morphology to M-TS-1, but the interlayer distance is much larger (~3.0 nm), due to the incorporation of SiO_2 and SiO_2/TiO_2 pillars between adjacent zeolitic layers. The 2D zeolitic layers in Si-TS-1 has more ordered structure than that of Si/Ti-TS-1 sample.

The N_2 isotherms and pore size distributions were measured on these TS-1 samples to understand their surface area and porosity properties. As shown in Figure 5a, at the relatively low pressures (for example, $P/P_0 < 0.02$), all TS-1 samples exhibit similar N_2 uptakes and thus similar microporosities. At a higher relative pressure range ($0.02 <$

P/P_0 < 0.9), the volume of N_2 adsorbed and the related mesoporosity increased significantly in the order of C-TS-1 < M-TS-1 < Si/Ti-TS-1 < Si-TS-1. The non-local density functional theory (NLDFT) pore size distributions (Figure 5b) further underscore the changes in the textural properties of the TS-1 zeolites. The plots of pore size distributions were determined from the adsorption branches of N_2 isotherms using cylindrical-type pore and zeolite adsorbent model. Broad peaks in the range of 2-5 nm with different intensities detected in these zeolite samples reflect the existence of different mesoporosities. The M-TS-1 has a broad and less intense peak, analogous to that of C-TS-1, suggesting the collapse of multilayer structure after calcination. The peak corresponding to mesopores was presented in both pillared TS-1 samples. When comparing the peak of Si-TS-1 to that of Si/Ti-TS-1, the former is much narrower and sharper, suggesting the formation of more uniform mesopores, when pillaring solvent does not contain TBOT. Table 1 summarizes the textural properties of all the C-TS-1, M-TS-1, Si-TS-1 and Si/Ti-TS-1 samples that were determined from the N_2 isotherms. It can be seen from Table 1 that the external surface area (S_{ext}), mesopore volume (V_{meso}), total pore volume (V_t) and BET surface area (S_{BET}) were dramatically increased after pillaring treatment of M-TS-1(P) zeolite. Commensurately, the micropore surface area (S_{micro}) decreases after the pillarization of 2D TS-1 nanosheets into hierarchical meso-/microporous structures. The micropore volume (V_{micro}) kept nearly constant among the M-TS-1, Si-TS-1 and Si/Ti-TS-1 samples.

3.2. Composition and coordination status of Ti-atoms

Table 2 summarizes the Si and Ti contents in C-TS-1, M-TS-1, Si-TS-1 and Si/Ti-TS-1 zeolites. The Si/Ti ratios measured from the elemental analysis are similar to those shown in the synthesis recipes of C-TS-1 and M-TS-1 zeolites. The pillarization treatment with TEOS led to an increase in the Si/Ti ratio in the Si-TS-1 zeolite, while the usage of TEOS/TBOT mixture solvent decreased the Si/Ti ratio in Si/Ti-TS-1 zeolite, when compared to the reference M-TS-1 zeolite. From the Si/Ti ratio difference between M-TS-1 and Si-TS-1 zeolites, the amount of SiO_2 pillar introduced in Si-TS-1 was determined (shown in Table 2, calculation details referring to Section S1 in Supporting Information) to be 29 wt%. Similarly, the SiO_2 and TiO_2 contents in the pillars of Si/Ti-TS-1 were evaluated (Section S1 in Supporting Information). The Si/Ti ratio in pillars of Si/Ti-TS-1 is calculated to be 48, which is much lower than the starting Si/Ti ratio (i.e., 100) in the TEOS/TBOT mixture solvent. This indicates that TBOT, the Ti precursor, has a higher tendency than TEOS, the Si precursor, to be incorporated into the M-TS-1(P) zeolite, consistent with our previous report on SiO_2/TiO_2 pillared ZSM-5 lamellar zeolite[47]. Apparently, the interlayer pillars in Si/Ti-TS-1 contain higher concentration of Ti-sites than that of the zeolitic layers.

Figure 6 shows the DR UV-Vis spectra of these four TS-1 samples which were used to identify the coordination environment of Ti-sites. The C-TS-1 and M-TS-1 have comparable absorption peak features: one major peak centered at ~206 nm and a shoulder peak stayed around 229 nm. The sharp and narrow band at ~206 nm corresponds to Ti-species with tetrahedral coordination structure ($Ti(OSi)_4$) in the zeolite framework, while the shoulder peak is caused by the existence of tetrahedral, tripodal Ti species ($Ti(OH)(OSi)_3$).[30, 35, 48] The slightly higher intensity in the shoulder peak of M-TS-1

than that of C-TS-1 reflects that the former contains a slightly higher fraction of tetrahedral, tripodal Ti-atoms. The shrinkage of the TS-1 zeolite from 3D crystalline structure to 2D nanosheet (~ 3 nm thickness in *b*-axis direction) creates more defects in M-TS-1, and consequently forms slightly more extra-framework Ti species. The pillarization of M-TS-1(P) to form Si-TS-1 increases the SiO_2 contents, because SiO_2 pillars account for ~29 wt % of the sample weight, and decreases the Ti-site concentration commensurately, as confirmed from the decrease in the peak intensities at ~206 and ~229 nm after the SiO_2 pillaring treatment. It should be noted that the pillarization by TEOS created a small amount of non-tetrahedrally coordinated Ti-atoms, reflected by the slight increase in the peak intensity in the region of 280 – 330 nm in its DR UV-vis spectrum (higher than that of C-TS-1 in this region). The pillarization of M-TS-1(P) with SiO_2/TiO_2 apparently forms more types of coordination states of Ti-sites in the pillars between two adjacent zeolitic layers. Besides the peaks at ~206 and ~229 nm, two more peaks located at ~272 and ~328 nm appeared. These new peaks correspond to octahedral coordination state ($Ti(OH)_2(H_2O)_2(OSi)_2$)) and anatase-like TiO_2.[17, 19, 20, 49-51] The overall spectrum of Si/Ti-TS-1 zeolite has a higher intensity than other samples due to increased Ti-site concentration (Table 2). This SiO_2/TiO_2 pillarization process led to a higher Ti-site concentration and diverse types of Ti-coordination structures.

A Gaussian curve fitting program (Peakfit software) was used to deconvolute these DR UV-vis peaks. Figure S1 in Supporting Information shows the deconvoluted peaks and the fitted peaks for all these four TS-1 zeolites. Four peaks centered at 206, 229, 272 and 328 nm, corresponding to the tetrahedral tetrapodal $Ti(OSi)_4$, tetrahedral

tripodal $Ti(OH)(OSi)_3$, octahedrally coordinated $Ti(OH)_2(H_2O)_2(OSi)_2$ and anatase-like TiO_2 structures[48, 52-54], respectively, were obtained. The peak area at each location was integrated and normalized to that of the entire spectrum. Table 3 summarizes the peak area percentage in each TS-1 zeolite, reflecting the relative quantity of each coordination environment of Ti-sites. Clearly, from C-TS-1 to M-TS-1 and Si-TS-1, the percentage of tetrahedrally coordinated tetrapodal Ti-atoms decreases slightly. The Si/Ti-TS-1 has ultra-high percentage of extra-framework octahedrally coordinated Ti-atoms and anatase-like TiO_2 than the 3D (C-TS-1) and other 2D (M-TS-1 and 2D Si-TS-1) zeolites.

3.3. Confinement environment of silanol and titanol groups

The local environment and extent of confinement of silanol (Si-OH) and titanol (Ti-OH) groups in 3D C-TS-1 and hierarchical 2D M-TS-1, Si-TS-1 and Si/Ti-TS-1 zeolites are analyzed by the hydroxyl vibration (ν(OH)) in the 3000-4000 cm^{-1} region of their DRIFT spectra, as shown in Figure 7. Three bands centered at 3740, 3675 and 3520 cm^{-1}, respectively, were observed. The band at 3740 cm^{-1} corresponds to the stretching vibration of ν(OH) in isolated Si-OH and Ti-OH groups, located at the external surface and within the zeolite micropores[51, 55-57], where they are not confined by either the shallow cavities on external surface or micropores. Next, the peak at 3675 cm^{-1} is assigned to the H-bonded Si-OH and Ti-OH groups that are partially confined in micropores and shallow cavities on external surfaces.[55-58] The broad band centered at 3520 cm^{-1} is associated with Si-OH and Ti-OH groups with strong and mutual H-bonding that exist in micropores or on external surface.[55, 58, 59] It is clearly seen that C-TS-1 has the highest concentrations of confined Si-OH and Ti-OH groups among all

samples. M-TS-1 has partially collapsed 2D zeolitic layers (Figure 1) and therefore higher concentrations of free isolated Si-OH and Ti-OH groups than C-TS-1. After pillarization treatment, Si-TS-1 and Si/Ti-TS-1 zeolites acquire the highest concentrations of the free, isolated Si-OH and Ti-OH groups than M-TS-1 and C-TS-1 zeolites, because pillarization treatments create more mesopore walls and thus generate more external surfaces on the 2D nanosheets that are terminated by these Si-OH and Ti-OH groups[60].

For each TS-1 zeolite, the peaks corresponding to Si-OH and Ti-OH groups in different confinement extents was normalized to the Si-O-Si overtone band at 2000 cm^{-1} and then deconvoluted (Figure S2) to obtain their areas by integration. The peak areas were then divided by the total peak area in the 3000-4000 cm^{-1} region to obtain their respective percentage, assuming that these species exhibit identical extinction coefficients. Table 4 summarizes the fraction of each type of Si-OH and Ti-OH species in their confined and unconfined environments within the zeolite samples. Overall, all four TS-1 zeolites have a mixture of unconfined and confined Ti-OH and Si-OH species, but the fraction of unconfined -OH species decreases according to the following order of Si/Ti-TS-1 ~ Si-TS-1 > M-TS-1 > C-TS-1.

3.4. Quantification for the concentration and strength of Lewis acidic Ti-sites

FTIR spectra of adsorbed pyridine were firstly collected to identify the nature of acid sites in each TS-1 zeolite, following previously established methods [61, 62]. Figure 8 shows spectra of adsorbed pyridine of C-TS-1, M-TS-1, Si-TS-1 and Si/Ti-TS-1 samples. The absence of an absorption band centered at 1550 cm^{-1}, which is ascribed to protonated pyridinium ions[37, 58, 63, 64], confirms that these samples do not contain any Brønsted acid site. Instead, the absorption feature at 1446 cm^{-1} confirms the presence

of Lewis sites [65-67]. We did not infer, from the peak intensity in Figure 8, on the actual or relative Lewis acid site concentration, because of the difficulty in determining the accurate extinction coefficient for each sample.

Instead, the concentration of Lewis acidic Ti-sites was quantified with pyridine chemical titration at 373 K. The validity of this method was carrying out the titration on the proton-form ZSM-5 (Zeolyst, CBV 8014) and commercial Aeroxide®P25 titania (TiO_2) samples (details refer to Section S4 of the Supporting Information). Figure 9a shows the Lewis acid site concentration in each TS-1 sample measured by the pyridine titration method. At 373 K, C-TS-1, M-TS-1, Si-TS-1 and Si/Ti-TS-1 contain 133.7, 102.2, 74.9 and 61.4 μmol g^{-1} of Lewis acid sites, respectively. Taken together with the Ti content in 3D C-TS-1, determined from elemental analysis, of 149.1 μmol g^{-1} (Table 5), the pyridine uptake gives the ratio of Lewis acid sites to Ti content of 89.7% (Figure 9b). This ratio is consistent with the percentage of tetrahedrally coordinated tetrapodal Ti-sites in C-TS-1, as shown in Figure 6 and Table 3, further confirming that the pyridine titration method allows quantitative counting of all Lewis acid sites in the framework of TS-1 zeolites. Following the same calculation method, the Lewis acid site-to-Ti ratios in M-TS-1, Si-TS-1 and Si/Ti-TS-1 were 70.6%, 79.4% and 25.6%, respectively. The slight decrease in the Lewis acid site concentrations (Figure 9a) and the ratio of Lewis acid site-to-Ti content (Figure 9b) in M-TS-1 and Si-TS-1, compared to those of C-TS-1, indicate that the hierarchical 2D TS-1 zeolites have weaker acidity than 3D C-TS-1 zeolite. This is reflected by the slight increase in the percentages of non-tetrahedrally coordinated tetrapodal Ti-sites in both M-TS-1 and Si-TS-1 zeolites (Figure 6 and Table 3). The significant drop in Lewis acid site concentration (or Lewis acid site-to-Ti ratio) in Si/Ti-

TS-1 suggests that the SiO_2/TiO_2 pillarization not only created non-tetrahedrally coordinated tetrapodal Ti-sites in pillars but also distorted a portion of the tetrahedral coordination environment of Ti-sites in zeolitic layers. The distortion of Ti-sites in zeolitic layers is reasoned from the Ti content in both zeolitic layers and SiO_2/TiO_2 pillars in Si/Ti-TS-1, where the zeolitic layers have framework Ti-site densities similar to that of M-TS-1. Overall, this is consistent with the high percentages of extra-framework, octahedrally coordinated Ti-sites and anatase-like TiO_2 in Si/Ti-TS-1 after the SiO_2/TiO_2 pillarization post-synthesis treatment.

The strength of Lewis acidity in these TS-1 zeolites was further probed by measuring pyridine uptakes at 423 K (Figure 9a) and compared to that adsorbed at 373 K (Figure 9b). First of all, the pyridine uptakes at 423 K on all samples are less than those measured at 373 K. The ratios of pyridine adsorbed at 423 K to that at 373 K were 57.0%, 59.6%, 50.5% and 76.9%, respectively, in C-TS-1, M-TS-1, Si-TS-1 and Si/Ti-TS-1. The lower pyridine uptakes at the higher temperature suggests that pyridine does not adsorb on all Lewis sites at the higher temperature, likely because a portion of the Lewis sites has a weaker acid strength. For instance, FTIR studies of adsorbed pyridine on ZSM-5 zeolites have established that the pyridine adsorbs much more weakly on Lewis than Brønsted sites and, for this reason, the amount of pyridine adsorbed on Lewis sites decreases markedly as the adsorption temperature increases.[68-71] The same trend has been observed by the FTIR studies of adsorbed pyridine on TS-1 zeolites by Shamzhy et al[40]. Secondly, a close examination on the various descriptors of acid strength, represented either by the acid site-to-Ti ratio, based on pyridine titration at 373 K, or the pyridine uptake at 423 K over that at 373 K (Figure 9b), reveal that a small

variation exists among C-TS-1, M-TS-1 and Si-TS-1 zeolites. The Si/Ti-TS-1 zeolite, however, has a very different acid strength from the other three TS-1 materials. The derivation of M-TS-1 and Si-TS-1 from the same precursor material and no inclusion of Ti-sites in the post-synthesis treatment should contribute to the small variation in acidity strengths between M-TS-1 and Si-TS-1 zeolites. As noted by Shamzhy et al. in their FTIR studies of adsorbed pyridine in Si/Ti-TS-1 zeolite[40], the $Ti(OH)(OSi)_3$ group could form on the external surface of the TS-1 layers in the post-treatment, which causes a different acidity strength than other 2D TS-1 or 3D C-TS-1 materials.

3.5. In-situ acid site titration and catalytic properties of external Lewis acid sites

3.5.1 In-situ Lewis acid site titration by MPA titrant molecules

As noted in Section 2.5.1. above, epoxidation of C_8H_{14} exclusively occurs on the Ti_{ext} sites in TS-1 zeolite, because C_8H_{14} cannot access the Ti-sites located within the micropores (Ti_{int}), as confirmed in our previous publication[29]. The organic MPA titrant molecule has a kinetic diameter of ~0.65 nm that is larger than the micropore (0.51×0.55 nm along *a*-axis and 0.53×0.56 nm along *b*-axis) of TS-1 zeolite. Therefore, MPA selectively adsorbs on and titrates the Ti_{ext} sites, including those present within the mesopores, on external geometric surface of TS-1 particles and on surface of TiO_2/SiO_2 pillars (for the case of Si/Ti-TS-1 zeolite), making Ti_{ext} sites unreactive for epoxidation catalysis in the C_8H_{14}-H_2O_2 reaction mixture. The in-situ MPA titration study provided a direct, quantitative assessment on the relative abundance of the external Lewis sites in the 2D TS-1 zeolites. The section of MPA as the titrant is due to its strong interaction with

Lewis acid sites on solid catalysts, including Ti-sites in both zeolite[72, 73] and metal oxide[74] materials.

Figure 10 shows the normalized C_8H_{14} epoxidation rates, defined as the C_8H_{14} conversion rates measured with different MPA quantities over that measured without MPA added, as a function of the quantity of MPA added into the reaction mixtures, expressed in terms of the MPA-to-Ti site ratio (i.e. MPA/Ti (%)), for the four catalyst samples. The normalized epoxidation rates decreased proportionally as the MPA/Ti ratio increased, but as the normalized rates approached zero, where the added MPA titrated nearly all the active external Ti sites, the normalized rates deviated from this linearly trend in rate decrease. Bulky, pre-adsorbed MPA at the sites may hinder the diffusion of other MPAs and impose steric hindrance of another MPA to adsorb on neighboring sites. The x-axis intercepts, determined by extrapolating the normalized rates to zero, reflect the case of complete coverages of Ti_{ext} by MPA. Since each MPA occupies one site, these MPA-to-Ti ratios equal to the fractions of external Ti-site in each TS-1 catalyst, as indicated by dotted lines in Figure 10. The fractions of external Ti-sites are 7.1, 26.8, 63.3 and 37.7% for C-TS-1, M-TS-1, Si-TS-1 and Si/Ti-TS-1, respectively. These fractions, together with the Lewis acid site density determined by pyridine titration at 373 K, give the concentrations of external active Ti-sites, shown in the last column of Table 5. The increase in the concentration of Ti_{ext}-sites parallels the increase in zeolite mesoporosity, as expected, as summarized in Table 2.

3.5.2 Catalytic properties of external Lewis acidic Ti-sites in 2D TS-1 zeolites

Previous studies[18-20, 29] focused only on comparing the alkene conversions on hierarchical TS-1 zeolites. In contrast to these studies, we aimed to analyze the entire

reaction network, accounting for all reactions involving C_8H_{14} and H_2O_2, deciphering the individual rates and connecting these rates to the different types of active Ti-sites in hierarchical 2D TS-1 zeolites.

As shown in Figure 2, three reaction pathways lead to H_2O_2 decomposition, while only the first pathway consumes C_8H_{14}. In order to understand the catalytic property of external Ti-sites in epoxidation of C_8H_{14}, however, we need to resolve all three reaction pathways because H_2O_2 is the other reactant involved in C_8H_{14} reaction. The individual rates of the three reaction pathways are:

$$r_{epo} = -\frac{dC_{C_8H_{14}}}{dt} = k_{epo} M_L f_{L,ext} C_{C_8H_{14}} C_{H_2O_2} \quad (1)$$

$$r_{de,cat} = -\frac{dC_{H_2O_{2(2)}}}{dt} = k_{de,cat} M_L C_{H_2O_2} \quad (2)$$

$$r_{de,sel} = -\frac{dC_{H_2O_{2(3)}}}{dt} = k_{de,sel} C_{H_2O_2} \quad (3)$$

where r_{epo}, $r_{de,cat}$ and $r_{de,sel}$ are the reaction rates (mol L^{-1} s^{-1}) for C_8H_{14} epoxidation, catalytic H_2O_2 decomposition and non-catalytic thermal decomposition of H_2O_2 via Pathways (1)-(3), respectively. $C_{C_8H_{14}}$ is the cyclooctene concentration in solution (mol L^{-1}); $C_{H_2O_2}$ is H_2O_2 concentration in solution (mol L^{-1}); t is the reaction time (s); M_L (mol Ti) is the total number of mole of Lewis acidic Ti-sites used in each experiment, determined by pyridine titration at 373 K; $f_{L,ext}$ is the percentage of external Ti-sites (Table 5); k_{epo}, $k_{de,cat}$ and $k_{de,sel}$ are the rate constant for epoxidation (per external surface Lewis acid site (L mol^{-1}) [mol Ti_{ext}]$^{-1}$ s^{-1}), for catalytic H_2O_2 decomposition (per Lewis acid site, [mol Ti_{total}]$^{-1}$ s^{-1}) and for H_2O_2 thermal self-decomposition (s^{-1}), respectively. The term of

$M_L f_{L,ext}$ in equation (1) accounts for the fact that only external Ti-sites in TS-1 zeolites contribute to the epoxidation reaction. The $-\frac{dC_{H_2O_{2(2)}}}{dt}$ and $-\frac{dC_{H_2O_{2(3)}}}{dt}$ in equations (2) and (3) stand for H_2O_2 consumption rates due to the reaction pathways (2) and (3), respectively, in Figure 10.

Because all three reaction pathways contribute to H_2O_2 consumption, the rate for net H_2O_2 consumption ($r_{H_2O_2}$, mol L^{-1} s^{-1}) in C_8H_{14}-H_2O_2 reactions equals the sum of the individual rates of the three pathways,

$$r_{H_2O_2} = -\frac{dC_{H_2O_{2(1-2-3)}}}{dt} = r_{epo} + r_{de,cat} + r_{de,sel}$$
$$= k_{de,sel}C_{H_2O_2} + k_{de,cat}M_L C_{H_2O_2} + k_{epo}M_L f_{L,ext} C_{C_8H_{14}} C_{H_2O_2}$$

(4)

where the subscript "1-2-3" in $-\frac{dC_{H_2O_{2(1-2-3)}}}{dt}$ term represents the consumption rate of H_2O_2 due the reaction pathways (1), (2) and (3) in this reaction. The rate for non-productive H_2O_2 consumption (due to thermal and catalytic decomposition, $r_{H_2O_2(de,sel+de,cat)}$, mol L^{-1} s^{-1}) in the absence of C_8H_{14} is

$$r_{H_2O_2(de,sel+de,cat)} = -\frac{dC_{H_2O_{2(2-3)}}}{dt} = k_{de,sel}C_{H_2O_2} + k_{de,cat}M_L C_{H_2O_2}$$

(5)

in which the subscript "2-3" in $-\frac{dC_{H_2O_{2(2-3)}}}{dt}$ term represents both reaction pathways (2) and (3) contribute to the rate of $r_{H_2O_2(de,sel+de,cat)}$ in the reaction. The integral formats of differential equations (3) and (5) are shown in equations (6) and (7) below.

$$-ln\frac{C_{H_2O_{2(3)}}}{C^0_{H_2O_2}} = k_{de,sel}t \quad (6)$$

$$-ln\frac{C_{H_2O_{2(2-3)}}}{C^0_{H_2O_2}} = \left(k_{de,sel} + k_{de,cat}M_L\right)t = k_1 t \quad (7)$$

where $C^0_{H_2O_2}$ is the initial H_2O_2 molar concentration (at t = 0 s) and $k_1 = k_{de,sel} + k_{de,cat}$.

In combination of differential equations (1) and (4), equation (8) can be obtained:

$$C^0_{C_8H_{14}} - C^0_{H_2O_2} + C_{H_2O_2} - C_{C_8H_{14}} = \frac{k_1}{k_2}\ln\left(\frac{C_{C_8H_{14}}}{C^0_{C_8H_{14}}}\right) \quad (8)$$

in which$C^0_{C_8H_{14}}$ is the initial C_8H_{14} molar concentration (at t = 0 s) and $k_2 = k_{epo}M_L f_{L,ext}$. Section S5 of Supporting Information illustrates the details on the rate equation derivation. The rate constants, $k_{de,sel}$, k_1 and k_2 can be evaluated from the kinetics data collected from epoxidation of C_8H_{14} in H_2O_2 in the absence of catalyst, absence of C_8H_{14} (with H_2O_2 as the sole reactant) and in the presence of both TS-1 catalyst and C_8H_{14}, respectively. Section of S6 of Supporting Information summarizes the details on the rate data analysis and rate constants determination.

Table 6 summarizes the rate constants for C_8H_{14} and H_2O_2 consumptions evaluated from the C_8H_{14}-H_2O_2 reactions. First, the rate constant for H_2O_2 thermal decomposition, $k_{de,sel}$, was determined from controlled experiments without any catalyst. It has a value of 5.03 × 10^{-6} s^{-1}. This rate constant for homogeneous H_2O_2 thermal decomposition will remain to be the same for all experiments across the different TS-1 catalysts. Next, the rate constant of non-productive catalytic H_2O_2 decomposition on Ti-sites ($k_{de,cat}$), obtained from the control experiments in the absence of C_8H_{14} reactant, increases from C-TS-1, M-TS-1 to Si-TS-1 zeolite. Finally, the rate constant of C_8H_{14} epoxidation (k_{epo}), obtained from catalytic C_8H_{14}-H_2O_2 reactions, exhibits an opposite trend to that of $k_{de,cat}$ on these three TS-1 zeolites. An exception occurs for the Si/Ti-TS-1 zeolite. It has an exceptionally high $k_{de,cat}$ and k_{epo} values than both the 3D (C-

TS-1) and other 2D (M-TS-1 and Si-TS-1) zeolites. These results indicate that the catalytic activity of Ti_{total}-sites for catalytic H_2O_2 decomposition follows the order of C-TS-1 < M-TS-1 < Si-TS-1 << Si/Ti-TS-1, whereas the activity of external Ti_{ext}-sites for C_8H_{14} epoxidation follows the sequence of Si-TS-1< M-TS-1 < C-TS-1 << Si/Ti-TS-1.

In TS-1 zeolites, the catalytic activity of Lewis sites is influenced by the type of Ti-atom coordination, the acid site strength and the confining environment. Previous studies[52, 53, 75-77] have reported that the framework tetrahedral tetrapodal $Ti(OSi)_4$ and tetrahedral tripodal $Ti(OSi)_3OH$ sites as well as extra-framework octahedrally coordinated $Ti(OH)_2(H_2O)_2(OSi)_2$ sites are all effective for alkene epoxidation. Indeed, the $Ti(OSi)_3OH$ and $Ti(OH)_2(H_2O)_2(OSi)_2$ sites are much more effective than that of framework $Ti(OSi)_4$ sites[52, 53, 76, 78]. For C-TS-1, M-TS-1 and Si-TS-1 zeolites, they all have similar percentages of each coordinated Ti-sites (see Section 3.2) and acid site strengths (discussed in Section 3.4). Therefore, the activity trend in C_8H_{14} epoxidation in these three zeolites is not likely attributed to the difference in Ti-site coordination type or acid site strength. The degree of partial confining environment of silanol and titanol groups in C-TS-1, M-TS-1 and Si-TS-1, as discussed in Section 3.3, however, follows the order of C-TS-1 > M-TS-1 > Si-TS-1, same as that of reactivity trend. The degree of partial confining environment of external Ti_{ext}-sites in these zeolites is likely to be equivalent to the degree of partial confining environment of silanol and titanol groups. Figure 11 shows the linear dependence between the catalytic activity of Ti_{ext}-site and the degree of partial confinement for silanol and titanol groups in C-TS-1, M-TS-1 and Si-TS-1 zeolites. This suggests that the Ti-site confining environment could be responsible for the observed activity trend in C_8H_{14} epoxidation reaction. The 2D TS-1 zeolite

nanosheet has shallow cavities in external surface than that of well crystallized 3D TS-1, and thus it has less degree of partial confinement for active Ti-sites and lower activity in C_8H_{14} epoxidation. It should be noted that the existence of partial confinement of 2D zeolite nanosheet surface has been recently reported by Katz group[57], and the surface site confinement can be used to control activity of grafted Ti^{4+}-centers on 2D SSZ-70 nanosheets in cyclohexene epoxidation. From the perspective of site confining effect (Figure 7) and acidity strength (Figure 9), Si/Ti-TS-1 should have the lowest activity among these four TS-1 zeolites. The ultra-high activity of Si/Ti-TS-1 in C_8H_{14} epoxidation, however, should be caused by the high concentrations of non-tetrahedrally coordinated Ti-sites, as shown in Table 3 and Figure 6 in Section 3.2 above. As mentioned previously, the epoxidation activity of non-tetrahedrally coordinated sites are much higher than that of framework $Ti(OSi)_4$ sites[52, 53, 76-78].

4. Conclusions

In summary, the local environment and catalytic property of Lewis acid sites in hierarchical 2D lamellar M-TS-1, Si-TS-1 and Si/Ti-TS-1 zeolites were studied by a combination of physicochemical property characterization and catalytic kinetics measurements. In comparison to 3D C-TS-1, the 2D M-TS-1, Si-TS-1 and Si/Ti-TS-1 have higher mesoporosity and higher concentrations of free isolated surface silanol and titanol groups, hinting diminishment of acid site confinement environment enclosed in micropores. All these 2D TS-1 zeolites have lower concentrations of strong Lewis Ti-sites than 3D C-TS-1. The accessibility of Ti-sites to bulky molecules, however, increases with increasing mesoporosity in the TS-1 zeolites.–The catalytic activity of

external Ti-site decreases with increasing mesoporosity from C-TS-1, M-TS-1 to Si-TS-1, which can be attributed to the lower degree of site confinement on the external surface of 2D TS-1 nanosheet than that of 3D analogue. Distinct from C-TS-1, M-TS-1 and Si-TS-1 zeolites, the Si/Ti-TS-1 has much higher C_8H_{14} epoxidation rate, which should be attributed to the high concentrations of extra-framework, octahedrally coordinated Ti-sites. The present study will guide in-depth studies for Lewis acidity and catalytic behavior in other 2D zeolite materials, a topic falling behind with Brønsted acidity of the same type of materials.

Acknowledgements:

This project is supported by National Science Foundation (CBET-1705284 and CBET-1928325). This material is based upon work supported by, or in part by, the U. S. Army Research Laboratory and the U. S. Army Research Office under contract/grant number: W911NF-17-1-0363. We thank Kyle Vollett for performing the pyridine FTIR measurements.

References:

[1] M. Taramasso, G. Perego, B. Notari, Preparation of porous crystalline synthetic material comprised of silicon and titanium oxides, US, (1983) US4410501A.

[2] A. Tuel, S. Moussa-Khouzami, Y.B. Taarit, C. Naccache, Hydroxylation of phenol over TS-1: surface and solvent effects, J. Mol. Catal., 68 (1991) 45-52.

[3] H. Liu, G. Lu, Y. Guo, Y. Guo, J. Wang, Chemical kinetics of hydroxylation of phenol catalyzed by TS-1/diatomite in fixed-bed reactor, Chem. Eng. J., 116 (2006) 179-186.

[4] A. Thangaraj, R. Kumar, P. Ratnasamy, Catalytic properties of crystalline titanium silicalites II. Hydroxylation of phenol with hydrogen peroxide over TS-1 zeolites, J. Catal., 131 (1991) 294-297.

[5] L. Yang, F. Xin, J. Lin, Z. Zhuang, R. Sun, Continuous heterogeneous cyclohexanone ammoximation reaction using a monolithic TS-1/cordierite catalyst, RSC Adv., 4 (2014) 27259-27266.

[6] S. Saxena, J. Basak, N. Hardia, R. Dixit, S. Bhadauria, R. Dwivedi, R. Prasad, A. Soni, G.S. Okram, A. Gupta, Ammoximation of cyclohexanone over nanoporous TS-1 using UHP as an oxidant, Chem. Eng. J., 132 (2007) 61-66.

[7] A. Thangaraj, S. Sivasanker, P. Ratnasamy, Catalytic properties of crystalline titanium silicalites III. Ammoximation of cyclohexanone, J. Catal., 131 (1991) 394-400.

[8] C. Dong, K. Wang, J.S. Zhang, G.S. Luo, Reaction kinetics of cyclohexanone ammoximation over TS-1 catalyst in a microreactor, Chem. Eng. Sci., 126 (2015) 633-640.

[9] X. Liu, X. Wang, X. Guo, G. Li, Effect of solvent on the propylene epoxidation over TS-1 catalyst, Catal. Today, 93-95 (2004) 505-509.

[10] G. Wu, Y. Wang, L. Wang, W. Feng, H. Shi, Y. Lin, T. Zhang, X. Jin, S. Wang, X. Wu, P. Yao, Epoxidation of propylene with H_2O_2 catalyzed by supported TS-1 catalyst in a fixed-bed reactor: Experiments and kinetics, Chem. Eng. J., 215-216 (2013) 306-314.

[11] L. Cumaranatunge, W.N. Delgass, Enhancement of Au capture efficiency and activity of Au/TS-1 catalysts for propylene epoxidation, J. Catal., 232 (2005) 38-42.

[12] D. Bianchi, L. Balducci, R. Bortolo, R. D'Aloisio, M. Ricci, G. Spanò, R. Tassinari, C. Tonini, R. Ungarelli, Oxidation of benzene to phenol with hydrogen peroxide catalyzed by a modified titanium silicalite (TS-1B), Adv. Synth. Catal., 349 (2007) 979-986.

[13] L. Balducci, D. Bianchi, R. Bortolo, R. D'Aloisio, M. Ricci, R. Tassinari, R. Ungarelli, Direct oxidation of benzene to phenol with hydrogen peroxide over a modified titanium silicalite, Angew. Chem. Int. Ed., 42 (2003) 4937-4940.

[14] T. Tatsumi, M. Nakamura, K. Yuasa, H.-o. Tominaga, Shape selective epoxidation of alkenes catalyzed by titanosilicate, Chem. Lett., 19 (1990) 297-298.

[15] M.G. Clerici, P. Ingallina, Epoxidation of lower olefins with hydrogen peroxide and titanium silicalite, J. Catal., 140 (1993) 71-83.

[16] C.-G. Li, Y. Lu, H. Wu, P. Wu, M. He, A hierarchically core/shell-structured titanosilicate with multiple mesopore systems for highly efficient epoxidation of alkenes, Chem. Commun., 51 (2015) 14905-14908.

[17] J. Kim, J. Chun, R. Ryoo, MFI zeolite nanosheets with post-synthetic Ti grafting for catalytic epoxidation of bulky olefins using H_2O_2, Chem. Commun., 51 (2015) 13102-13105.

[18] K. Na, C. Jo, J. Kim, W.-S. Ahn, R. Ryoo, MFI titanosilicate nanosheets with single-unit-cell thickness as an oxidation catalyst using peroxides, ACS Catal., 1 (2011) 901-907.

[19] J. Wang, L. Xu, K. Zhang, H. Peng, H. Wu, J.-g. Jiang, Y. Liu, P. Wu, Multilayer structured MFI-type titanosilicate: synthesis and catalytic properties in selective epoxidation of bulky molecules, J. Catal., 288 (2012) 16-23.

[20] J. Přech, P. Eliášová, D. Aldhayan, M. Kubů, Epoxidation of bulky organic molecules over pillared titanosilicates, Catal. Today, 243 (2015) 134-140.

[21] A. Wróblewska, A. Fajdek, Epoxidation of allyl alcohol to glycidol over the microporous TS-1 catalyst, J. Hazard. Mater., 179 (2010) 258-265.

[22] W. Jiao, Y. He, J. Li, J. Wang, T. Tatsumi, W. Fan, Ti-rich TS-1: A highly active catalyst for epoxidation of methallyl chloride to 2-methyl epichlorohydrin, Appl. Catal. A, 491 (2015) 78-85.

[23] Z. Deng, Y. Yang, X. Lu, J. Ding, M. He, P. Wu, Studies on the epoxidation of methallyl chloride over TS-1 microsphere catalysts in a continuous slurry reactor, Catal. Sci. Technol., 6 (2016) 2605-2615.

[24] J.-G. Wang, H. Wang, T. Yokoi, T. Tatsumi, Synthesis of Ti-containing extra-large-pore zeolites of Ti-CIT-5 and Ti-SSZ-53 and their catalytic applications, Micropor. Mesopor. Mat., 276 (2019) 207-212.

[25] K. Fu, H. Wang, T. Li, J.-G. Wang, Synthesis of Ti-containing 14-ring extra-large-pore zeolite of Ti-SFN and its catalytic application for bulky cycloalkene, Mater. Lett., 244 (2019) 10-12.

[26] J. Přech, J. Čejka, UTL titanosilicate: an extra-large pore epoxidation catalyst with tunable textural properties, Catal. Today, 277 (2016) 2-8.

[27] M. Mazur, V. Kasneryk, J. Přech, F. Brivio, C. Ochoa-Hernández, A. Mayoral, M. Kubů, J. Čejka, Zeolite framework functionalisation by tuneable incorporation of various metals into the IPC-2 zeolite, Inorg. Chem. Front., 5 (2018) 2746-2755.

[28] M. Choi, K. Na, J. Kim, Y. Sakamoto, O. Terasaki, R. Ryoo, Stable single-unit-cell nanosheets of zeolite MFI as active and long-lived catalysts, Nature, 461 (2009) 246.

[29] W. Wu, D.T. Tran, X. Wu, S.C. Oh, M. Wang, H. Chen, L. Emdadi, J. Zhang, E. Schulman, D. Liu, Multilamellar and pillared titanium silicalite-1 with long-range order of zeolite nanosheet layers: synthesis and catalysis, Micropor. Mesopor. Mat., 278 (2019) 414-422.

[30] A. Tuel, Crystallization of titanium silicalite-1 (TS-1) from gels containing hexanediamine and tetrapropylammonium bromide, Zeolites, 16 (1996) 108-117.

[31] A. Corma, V. Fornés, J.M. Guil, S. Pergher, T.L.M. Maesen, J.G. Buglass, Preparation, characterisation and catalytic activity of ITQ-2, a delaminated zeolite, Micropor. Mesopor. Mat., 38 (2000) 301-309.

[32] A. Corma, U. Díaz, V. Fornés, J. L. Jordá, M. Domine, F. Rey, Ti/ITQ-2, a new material highly active and selective for the epoxidation of olefins with organic hydroperoxides, Chem. Commun., 0 (1999) 779-780.

[33] N.A. Grosso-Giordano, C. Schroeder, A. Okrut, A. Solovyov, C. Schöttle, W. Chassé, N. Marinković, H. Koller, S.I. Zones, A. Katz, Outer-sphere control of catalysis on surfaces: a comparative study of Ti(IV) single-sites grafted on amorphous versus crystalline silicates for alkene epoxidation, J. Am. Chem. Soc., 140 (2018) 4956-4960.

[34] C.-C. Chang, J.-F. Lee, S. Cheng, Highly catalytically active micro/meso-porous Ti-MCM-36 prepared by a grafting method, J. Mater. Chem. A, 5 (2017) 15676-15687.

[35] F. Jin, C.-C. Chang, C.-W. Yang, J.-F. Lee, L.-Y. Jang, S. Cheng, New mesoporous titanosilicate MCM-36 material synthesized by pillaring layered ERB-1 precursor, J. Mater. Chem. A, 3 (2015) 8715-8724.

[36] D. Liu, X. Zhang, A. Bhan, M. Tsapatsis, Activity and selectivity differences of external Brønsted acid sites of single-unit-cell thick and conventional MFI and MWW zeolites, Micropor. Mesopor. Mat., 200 (2014) 287-290.

[37] Y. Wu, Z. Lu, L. Emdadi, S.C. Oh, J. Wang, Y. Lei, H. Chen, D.T. Tran, I.C. Lee, D. Liu, Tuning external surface of unit-cell thick pillared MFI and MWW zeolites by atomic layer deposition and its consequences on acid-catalyzed reactions, J. Catal., 337 (2016) 177-187.

[38] D. Liu, A. Bhan, M. Tsapatsis, S. Al Hashimi, Catalytic behavior of brønsted acid sites in MWW and MFI zeolites with dual meso- and microporosity, ACS Catal., 1 (2011) 7-17.

[39] L. Emdadi, S.C. Oh, Y. Wu, S.N. Oliaee, Y. Diao, G. Zhu, D. Liu, The role of external acidity of meso-/microporous zeolites in determining selectivity for acid-catalyzed reactions of benzyl alcohol, J. Catal., 335 (2016) 165-174.

[40] M. Shamzhy, J. Přech, J. Zhang, V. Ruaux, H. El-Siblani, S. Mintova, Quantification of Lewis acid sites in 3D and 2D TS-1 zeolites: FTIR spectroscopic study, Catal. Today,345 (2020), 80-87.

[41] R. Wei, H. Yang, J.A. Scott, K.-F. Aguey-Zinsou, D. Zhang, 2D versus 3D MFI zeolite: the effect of Si/Al ratio on the accessibility of acid sites and catalytic performance, Mater. Today Chem., 8 (2018) 1-12.

[42] L. Emdadi, Y. Wu, G. Zhu, C.-C. Chang, W. Fan, T. Pham, R.F. Lobo, D. Liu, Dual template synthesis of meso- and microporous MFI zeolite nanosheet assemblies with tailored activity in catalytic reactions, Chem. Mater., 26 (2014) 1345-1355.

[43] W.R. Gunther, V.K. Michaelis, R.G. Griffin, Y. Román-Leshkov, Interrogating the Lewis acidity of metal sites in beta zeolites with ^{15}N pyridine adsorption coupled with MAS NMR spectroscopy, J. Phys. Chem. C, 120 (2016) 28533-28544.

[44] G.P. Bienert, J.K. Schjoerring, T.P. Jahn, Membrane transport of hydrogen peroxide, BBA - Biomembranes, 1758 (2006) 994-1003.

[45] T. Henzler, E. Steudle, Transport and metabolic degradation of hydrogen peroxide in Chara corallina: model calculations and measurements with the pressure probe suggest transport of H_2O_2 across water channels, J. Exp. Bot., 51 (2000) 2053-2066.

[46] R.M. Sellers, Spectrophotometric determination of hydrogen peroxide using potassium titanium(IV) oxalate, Analyst, 105 (1980) 950-954.

[47] L. Emdadi, D.T. Tran, J. Zhang, W. Wu, H. Song, Q. Gan, D. Liu, Synthesis of titanosilicate pillared MFI zeolite as an efficient photocatalyst, RSC Adv., 7 (2017) 3249-3256.

[48] P. Ratnasamy, D. Srinivas, H. Knözinger, Active sites and reactive intermediates in titanium silicate molecular sieves, Advances in Catalysis, Academic Press 2004, pp. 1-169.

[49] H. Zhang, Y. Liu, Z. Jiao, M. He, P. Wu, Hydrothermal synthesis of titanium silicalite-1 structurally directed by hexamethyleneimine, Ind. Eng. Chem. Res., 48 (2009) 4334-4339.

[50] H.L. Chen, S.W. Li, Y.M. Wang, Synthesis and catalytic properties of multilayered MEL-type titanosilicate nanosheets, J. Mater. Chem. A, 3 (2015) 5889-5900.

[51] A. Zecchina, G. Spoto, S. Bordiga, A. Ferrero, G. Petrini, G. Leofanti, M. Padovan, Framework and extraframework Ti in titanium-silicalite: investigation by means of physical methods, in: P.A. Jacobs, N.I. Jaeger, L. Kubelková, B. Wichterlov´ (Eds.) Studies in Surface Science and Catalysis, Elsevier 1991, pp. 251-258.

[52] L. Wu, X. Deng, S. Zhao, H. Yin, Z. Zhuo, X. Fang, Y. Liu, M. He, Synthesis of a highly active oxidation catalyst with improved distribution of titanium coordination states, Chem. Commun., 52 (2016) 8679-8682.

[53] L. Wu, Z. Tang, Y. Yu, X. Yao, W. Liu, L. Li, B. Yan, Y. Liu, M. He, Facile synthesis of a high-performance titanosilicate catalyst with controllable defective $Ti(OSi)_3OH$ sites, Chem. Commun., 54 (2018) 6384-6387.

[54] S. Jin, Z. Wang, G. Tao, S. Zhang, W. Liu, W. Fu, B. Zhang, H. Sun, Y. Wang, W. Yang, UV resonance Raman spectroscopic insight into titanium species and structure-performance relationship in boron-free Ti-MWW zeolite, J. Catal., 353 (2017) 305-314.

[55] A. Zecchina, S. Bordiga, G. Spoto, L. Marchese, G. Petrini, G. Leofanti, M. Padovan, Silicalite characterization. 2. IR spectroscopy of the interaction of carbon monoxide with internal and external hydroxyl groups, J. Phys. Chem. C, 96 (1992) 4991-4997.

[56] N.A. Grosso-Giordano, A.S. Hoffman, A. Boubnov, D.W. Small, S.R. Bare, S.I. Zones, A. Katz, Dynamic reorganization and confinement of Ti^{IV} active sites controls olefin epoxidation catalysis on two-dimensional zeotypes, J. Am. Chem. Soc., 141 (2019) 7090-7106.

[57] I. Halasz, M. Agarwal, E. Senderov, B. Marcus, Continuous monitoring the oxyfunctionalization of hexane by aqueous H_2O_2 over TS-1 related catalysts, Appl. Catal. A, 241 (2003) 167-184.

[58] X. Ouyang, S.-J. Hwang, R.C. Runnebaum, D. Xie, Y.-J. Wanglee, T. Rea, S.I. Zones, A. Katz, Single-step delamination of a MWW borosilicate layered zeolite precursor under mild conditions without surfactant and sonication, J. Am. Chem. Soc., 136 (2014) 1449-1461.

[59] A. Corma, C. Corell, V. Fornés, W. Kolodziejski, J. Pérez-Pariente, Infrared spectroscopy, thermoprogrammed desorption, and nuclear magnetic resonance study of the acidity, structure, and stability of zeolite MCM-22, Zeolites, 15 (1995) 576-582.
[60] K. Na, M. Choi, W. Park, Y. Sakamoto, O. Terasaki, R. Ryoo, Pillared MFI zeolite nanosheets of a single-unit-cell thickness, J. Am. Chem. Soc., 132 (2010) 4169-4177.

[61] Y. Bai, L. Wei, M. Yang, H. Chen, S. Holdren, G. Zhu, D.T. Tran, C. Yao, R. Sun, Y. Pan, D. Liu, Three-step cascade over a single catalyst: synthesis of 5-(ethoxymethyl)furfural from glucose over a hierarchical lamellar multi-functional zeolite catalyst, J. Mater. Chem. A, 6 (2018) 7693-7705.

[62] Y. Yang, F. Lin, H. Tran, Y.-H. Chin, Butanal condensation chemistry catalyzed by Brønsted acid sites on polyoxometalate clusters, ChemCatChem, 9 (2017) 287-299.

[63] L. Wei, K. Song, W. Wu, S. Holdren, G. Zhu, E. Shulman, W. Shang, H. Chen, M.R. Zachariah, D. Liu, Vapor-phase strategy to pillaring of two-dimensional zeolite, J. Am. Chem. Soc., 141 (2019) 8712-8716.

[64] C. Jo, R. Ryoo, N. Žilková, D. Vitvarová, J. Čejka, The effect of MFI zeolite lamellar and related mesostructures on toluene disproportionation and alkylation, Catal. Sci. Technol., 3 (2013) 2119-2129.

[65] W.N.P. van der Graaff, C.H.L. Tempelman, E.A. Pidko, E.J.M. Hensen, Influence of pore topology on synthesis and reactivity of Sn-modified zeolite catalysts for carbohydrate conversions, Catal. Sci. Technol., 7 (2017) 3151-3162.

[66] C.A. Emeis, Determination of integrated molar extinction coefficients for infrared absorption bands of pyridine adsorbed on solid acid catalysts, J. Catal., 141 (1993) 347-354.

[67] M. Guisnet, P. Ayrault, C. Coutanceau, M. Fernanda Alvarez, J. Datka, Acid properties of dealuminated beta zeolites studied by IR spectroscopy, J. Chem. Soc., Faraday Trans., 93 (1997) 1661-1665.

[68] B. Chakraborty, B. Viswanathan, Surface acidity of MCM-41 by in situ IR studies of pyridine adsorption, Catal. Today, 49 (1999) 253-260.

[69] N.-Y. Topsøe, K. Pedersen, E.G. Derouane, Infrared and temperature-programmed desorption study of the acidic properties of ZSM-5-type zeolites, J. Catal., 70 (1981) 41-52.

[70] F. Jin, Y. Li, A FTIR and TPD examination of the distributive properties of acid sites on ZSM-5 zeolite with pyridine as a probe molecule, Catal. Today, 145 (2009) 101-107.

[71] T. Barzetti, E. Selli, D. Moscotti, L. Forni, Pyridine and ammonia as probes for FTIR analysis of solid acid catalysts, J. Chem. Soc., Faraday Trans., 92 (1996) 1401-1407.

[72] D.T. Bregante, N.E. Thornburg, J.M. Notestein, D.W. Flaherty, Consequences of Confinement for Alkene epoxidation with hydrogen peroxide on highly dispersed group 4 and 5 metal oxide catalysts, ACS Catal., 8 (2018) 2995-3010.

[73] D.T. Bregante, A.M. Johnson, A.Y. Patel, E.Z. Ayla, M.J. Cordon, B.C. Bukowski, J. Greeley, R. Gounder, D.W. Flaherty, Cooperative effects between hydrophilic pores and solvents: catalytic consequences of hydrogen bonding on alkene epoxidation in zeolites, J. Am. Chem. Soc., 141 (2019) 7302-7319.

[74] R. Eaton Todd, M. Boston Andrew, B. Thompson Anthony, A. Gray Kimberly, M. Notestein Justin, Counting active sites on titanium oxide–silica catalysts for hydrogen peroxide activation through in situ poisoning with phenylphosphonic acid, ChemCatChem, 6 (2014) 3215-3222.

[75] M. Li, Y. Wang, Y. Wu, M. Wang, D. Zhou, Structure and catalytic activity of a newly proposed titanium species in a Ti-YNU-1 zeolite: a density functional theory study, Catal. Sci. Technol., 7 (2017) 4105-4114.

[76] L. Xu, D.-D. Huang, C.-G. Li, X. Ji, S. Jin, Z. Feng, F. Xia, X. Li, F. Fan, C. Li, P. Wu, Construction of unique six-coordinated titanium species with an organic amine ligand in titanosilicate and their unprecedented high efficiency for alkene epoxidation, Chem. Commun., 51 (2015) 9010-9013.

[77] D.H. Wells, W.N. Delgass, K.T. Thomson, Evidence of defect-promoted reactivity for epoxidation of propylene in titanosilicate (TS-1) catalysts: a DFT study, J. Am. Chem. Soc., 126 (2004) 2956-2962.

[78] Q. Guo, K. Sun, Z. Feng, G. Li, M. Guo, F. Fan, C. Li, A thorough investigation of the active titanium species in TS-1 zeolite by in situ UV resonance Raman spectroscopy, Chem. Eur. J., 18 (2012) 13854-13860.

List of Tables:

Table 1. Textural properties of C-TS-1, M-TS-1, Si-TS-1 and Si/Ti-TS-1 zeolites determined from N_2 adsorption-desorption isotherms.

Zeolite	V_{micro} [a] (cm^3g^{-1})	S_{micro} [a] (m^2g^{-1})	S_{BET} [b] (m^2g^{-1})	S_{ext} [c] (m^2g^{-1})	V_t [d] (cm^3g^{-1})	V_{meso} [e] (cm^3g^{-1})
C-TS-1	0.121	308	464	156	0.236	0.115

M-TS-1	0.113	263	466	203	0.452	0.339
Si-TS-1	0.118	120	595	475	0.521	0.403
Si/Ti-TS-1	0.108	137	514	377	0.452	0.344

[a]Determined from t-plot method; [b]Determined from Brunauer, Emmett, and Teller (BET) method; [c]Calculated by $S_{ext} = S_{BET} - S_{micro}$; [d]Calculated from N_2 adsorption at $P/P_0=0.95$; [e]Determined using $V_{meso} = V_t - V_{micro}$.

Table 2. Composition analysis for C-TS-1, M-TS-1, Si-TS-1 and Si/Ti-TS-1 zeolites.

Zeolite	Zeolite layer		Si/Ti ratio in overall particle[a]	Interlayer pillar		Weight gain due to pillarization (wt%)
	Si/Ti ratio used in synthesis	Si/Ti ratio in zeolite layer		TEOS/TBOT ratio[b]	Si/Ti ratio[c]	
C-TS-1	100	-	108	-	-	-
M-TS-1	100	101	101	-	-	-
Si-TS-1	100	101	147	∞	∞	29
Si/Ti-TS-1	100	101	75	100	48	29[d]

[a]Determined by ICP-OES analysis; [b]Molar ratio of TEOS/TBOT in the mixed alkoxide solvent; [c]Refer to S1 in Supporting Information; [d] Assumed to be the same as that of Si-TS-1.

Table 3. Quantification for Ti-sites with different coordination environments in C-TS-1, M-TS-1, Si-TS-1 and Si/Ti-TS-1 zeolites.

zeolite	$Ti(OSi)_4$ (%)	$Ti(OSi)_3OH$ (%)	$Ti(OH)_2(H_2O)_2(OSi)_2$ (%)	Anatase-like TiO_2 (%)
C-TS-1	90.12	9.88	0.00	0.00
M-TS-1	80.34	18.64	0.00	1.02
Si-TS-1	85.74	8.55	4.84	0.87
Si/Ti-TS-1	25.54	57.25	14.16	3.05

Table 4. Quantification for –OH group in silanol and titanol groups in different environments in C-TS-1, M-TS-1, Si-TS-1 and Si/Ti-TS-1 zeolites.

zeolite	Free isolated (-OH) (%)	Slightly bonded (-OH) (%)	Mutually bonded (-OH) (%)
C-TS-1	22.77	6.81	70.42
M-TS-1	49.04	12.04	38.92

Si-TS-1	60.28	39.72	0.00
Si/Ti-TS-1	60.73	39.27	0.00

Table 5. Quantification for Ti-sites in different locations of C-TS-1, M-TS-1, Si/Ti-TS-1 and Si-TS-1 zeolites.

Zeolite	$C_{Ti,ICP}$ [a] ($\mu mol\ g^{-1}$)	$C_{Ti,423K}$ [b] ($\mu mol\ g^{-1}$)	$C_{Ti,373K}$ [c] ($\mu mol\ g^{-1}$)	$f_{L,ext}$ [d] (%)	$C_{Ti,int}$ [e] ($\mu mol\ g^{-1}$)	$C_{Ti,ext}$ [f] ($\mu mol\ g^{-1}$)
C-TS-1	149.1	76.2	133.7	7.1	124.2	9.5
M-TS-1	144.7	60.9	102.2	26.8	74.8	27.4
Si-TS-1	94.3	37.8	74.9	63.3	27.5	47.4
Si/Ti-TS-1	240.1	47.2	61.4	37.7	38.2	23.1

[a]*Determined by ICP-OES analysis; Measured by pyridine titration at 423 K;* [c]*Measured by pyridine titration at 373K.* [d]*Determined by active site poisoning by MPA during C_8H_{14} epoxidation reaction;* [e]*Internal active Ti-sites, $C_{Ti,int} = C_{Ti,373K} \times (1 - \frac{f_{L,ext}}{100})$;* [f]*External active Ti-sites, $C_{Ti,ext} = C_{Ti,373K} \times f_{L,ext}$.*

Table 6. Rate constants of C_8H_{14} epoxidation and H_2O_2 decomposition in C_8H_{14}-H_2O_2 reactions on C-TS-1, M-TS-1, Si/Ti-TS-1 and Si-TS-1 zeolites.

	M_L ($\times 10^{-6}$ mol)[a]	$k_{de,sel}$ ($\times 10^{-6}\ s^{-1}$)[b]	k_1 ($\times 10^{-6}\ s^{-1}$)[c]	$k_{de,cat}$ ($\times 10^{-1}$ [mol Ti_{total}]$^{-1}\ s^{-1}$)[d]	$\frac{k_1}{2}$	k_2 ($\times 10^{-6}$ L $mol^{-1}\ s^{-1}$)	k_{epo} (($L\ mol^{-1}$) [mol Ti_{ext}]$^{-1}\ s^{-1}$)[e]
C-TS-1	6.69	5.03	7.22	3.28	3.13	2.31	4.87
M-TS-1	5.11	5.03	8.17	6.14	1.50	5.45	3.98
Si-TS-1	3.74	5.03	18.72	36.58	2.52	6.21	3.14
Si/Ti-TS-1	3.07	5.03	40.86	116.81	0.37	110.02	95.13

[a]*Calculated by $M_L = C_{Ti,373K} \times 0.050\ g\ catalyst$;* [b]*Rate constant of unproductive H_2O_2 thermal decomposition;* [c] $k_1 = k_{de,sel} + k_{de,cat} M_L$; [d]*Calculated by $k_{de,cat} = \frac{k_1 - k_{de,sel}}{M_L}$;* [e]*Calculated by $k_{epo} = \frac{k_2}{M_L f_{L,ext}}$.*

List of Figures:

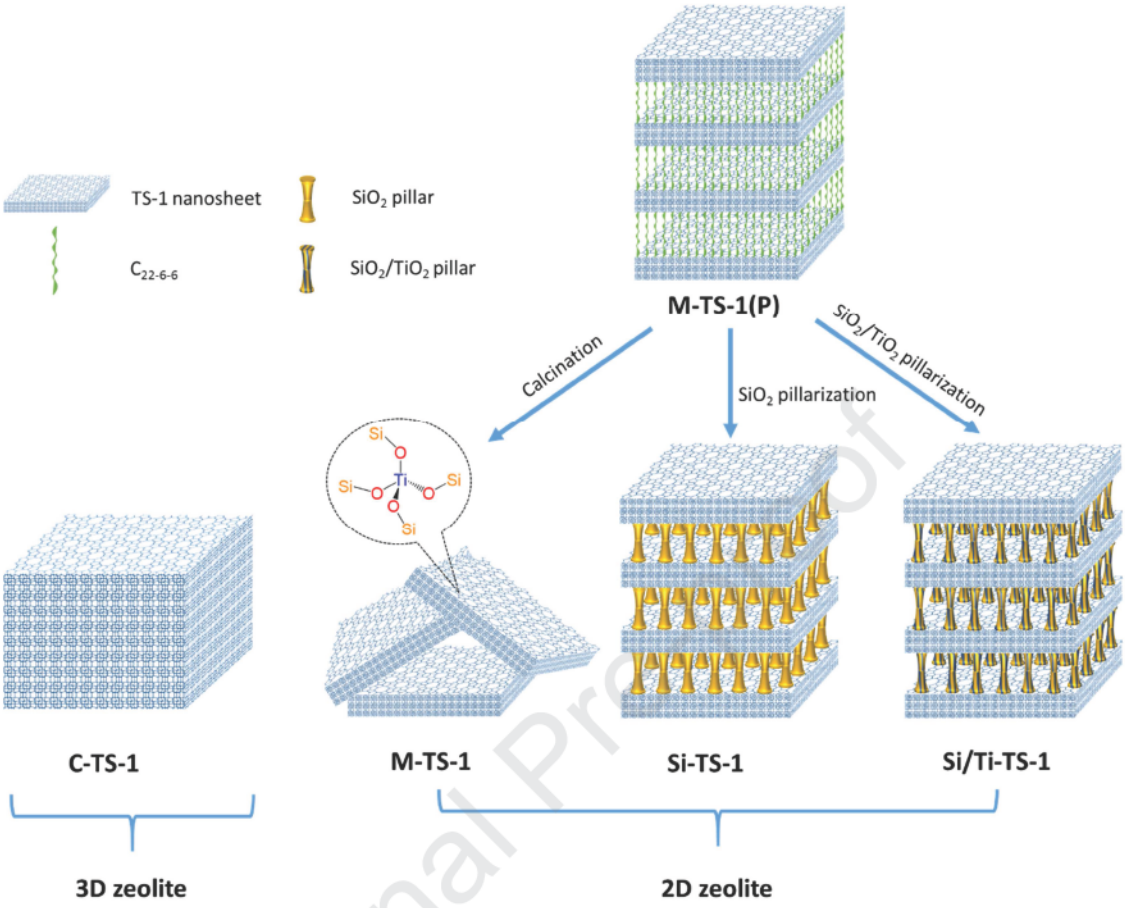

Figure 1. Schematic representation of the synthesized C-TS-1, M-TS-1, M-TS-1(P), Si-TS-1 and Si/Ti-TS-1 samples, respectively.

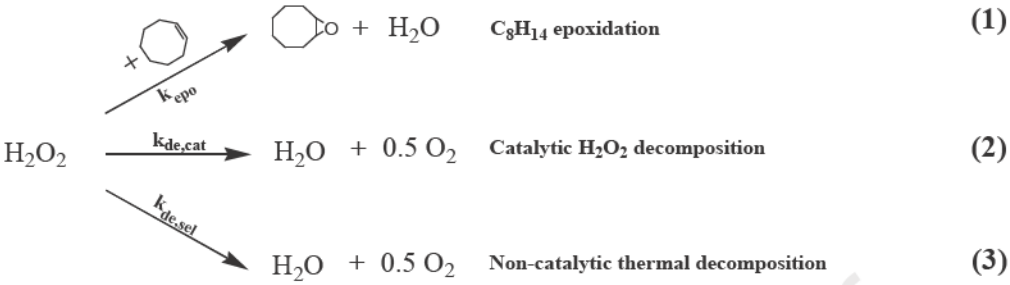

Figure 2. Reaction scheme of H_2O_2 consumption in epoxidation of C_8H_{14} with H_2O_2. (k_{epo}: *rate constant of H_2O_2 consumption in epoxidation of C_8H_{14}; $k_{de,cat}$: rate constant of H_2O_2 consumption caused by catalytic Ti sites; $k_{de,sel}$: rate constant of H_2O_2 consuption caused by thermal decomposition.*)

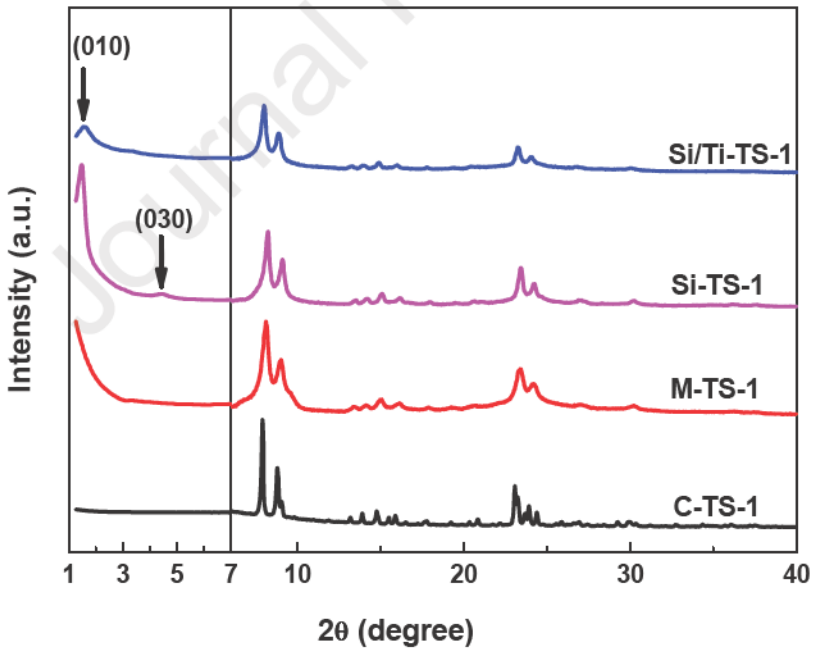

Figure 3. Low-angle and wide-angle XRD patterns of synthesized C-TS-1, M-TS-1, Si-TS-1 and Si/Ti-TS-1 samples, respectively.

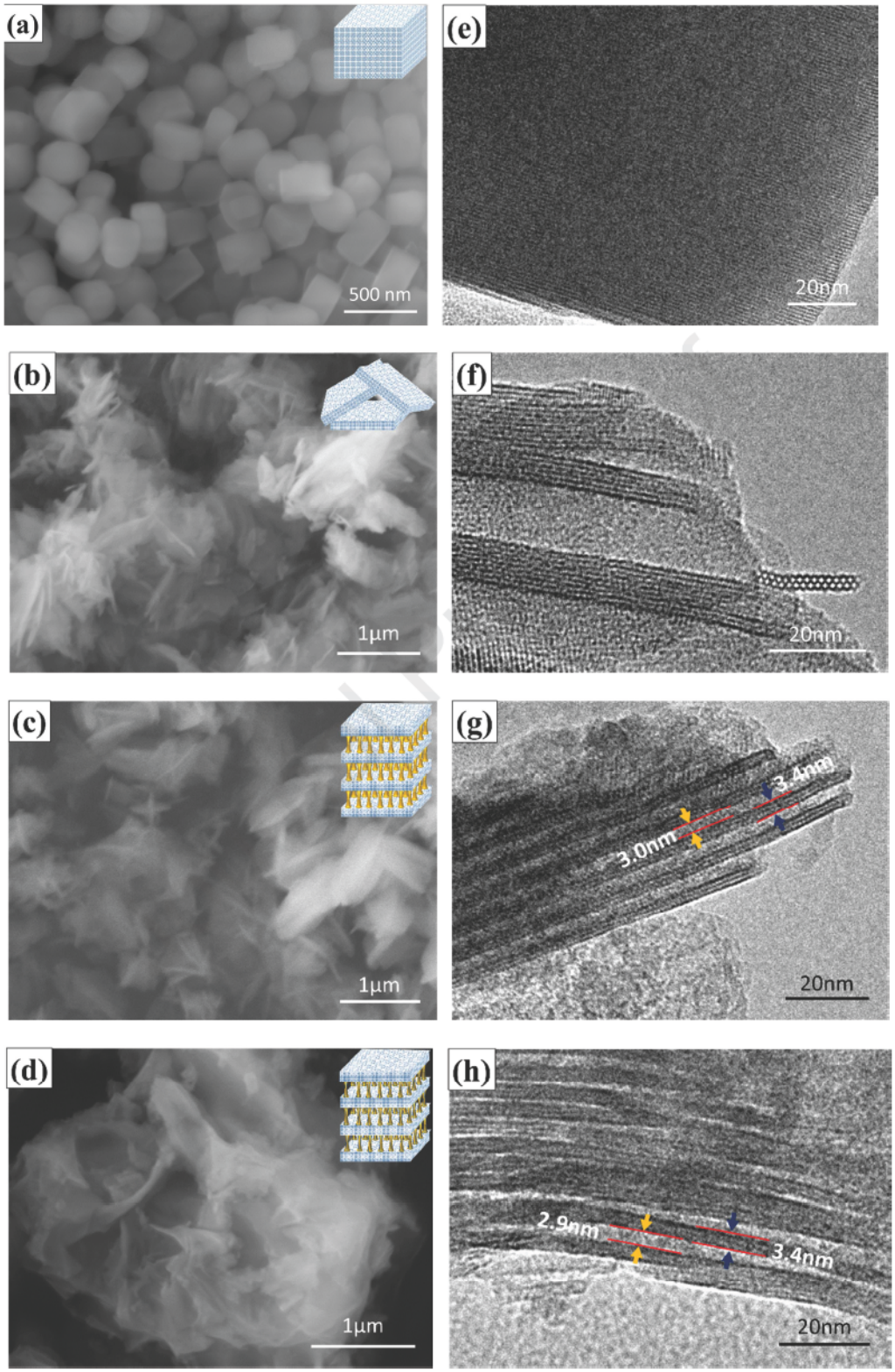

Figure 4. SEM (on the left side) and TEM (on the right side) images of C-TS-1(a, e), M-TS-1(b, f), Si-TS-1(c, g) and Si/Ti-TS-1(d, h) samples, respectively.

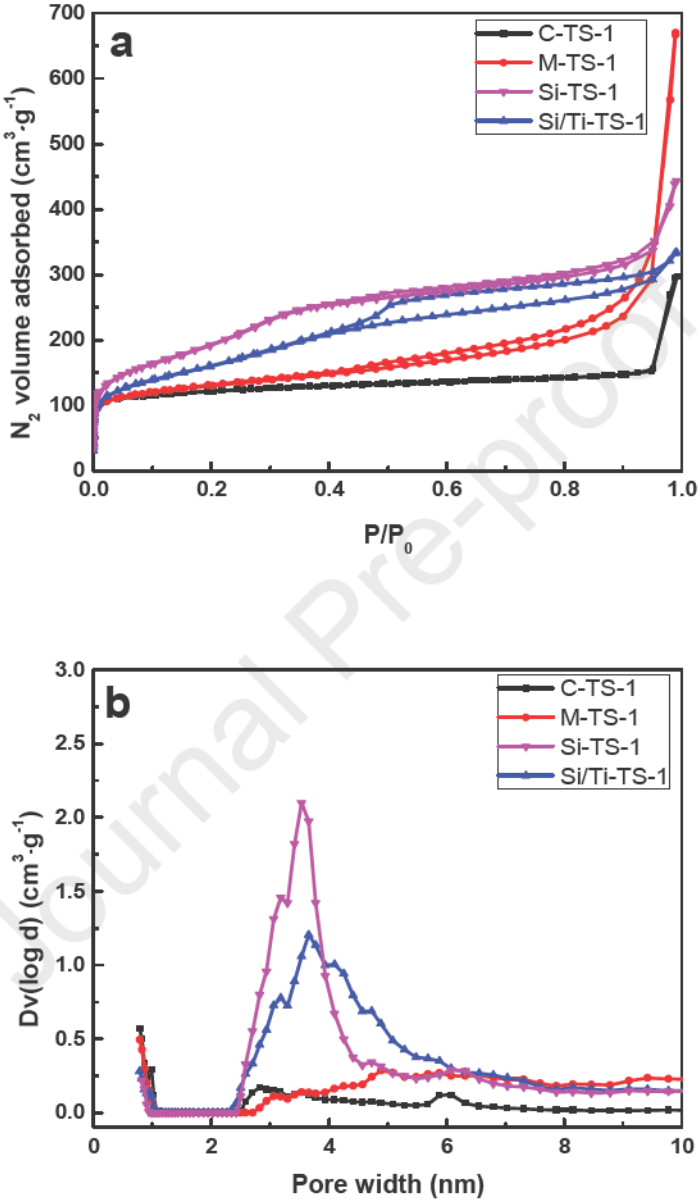

Figure 5. N_2 isotherms (a) and NLDFT pore size distributions (b) of C-TS-1, M-TS-1, Si-TS-1, and Si/Ti-TS-1 samples, respectively.

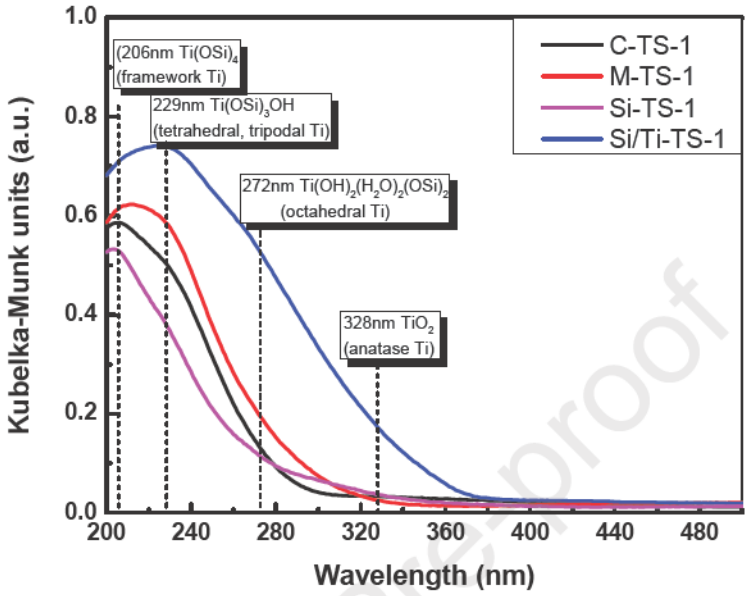

Figure 6. DR UV-Vis spectra of C-TS-1, M-TS-1, Si-TS-1 and Si/Ti-TS-1 samples, respectively.

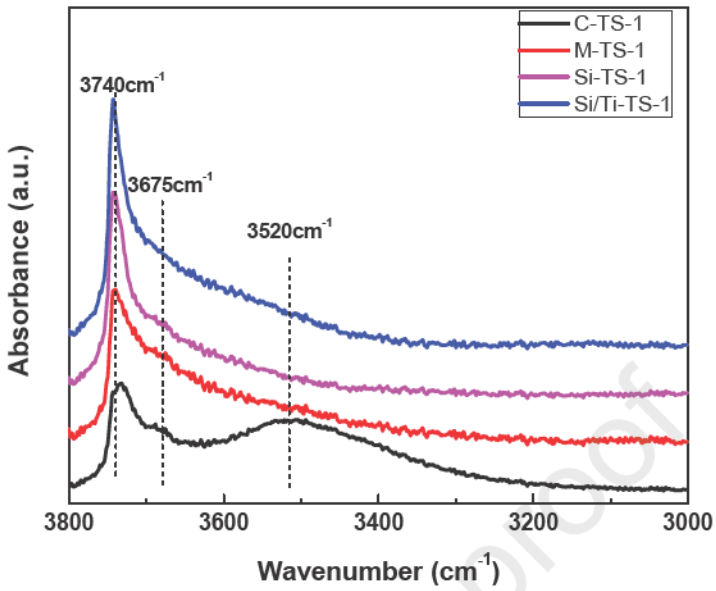

Figure 7. DRIFTS spectra of –OH groups in C-TS-1, M-TS-1, Si-TS-1 and Si/Ti-TS-1 zeolites, respectively.

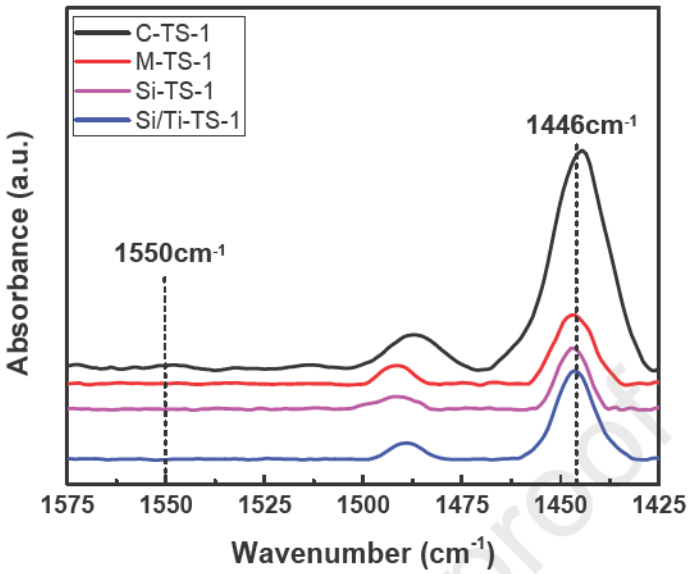

Figure 8. FTIR spectra of pyridine adsorbate on C-TS-1, M-TS-1, Si-TS-1 and Si/Ti-TS-1 zeolites, respectively.

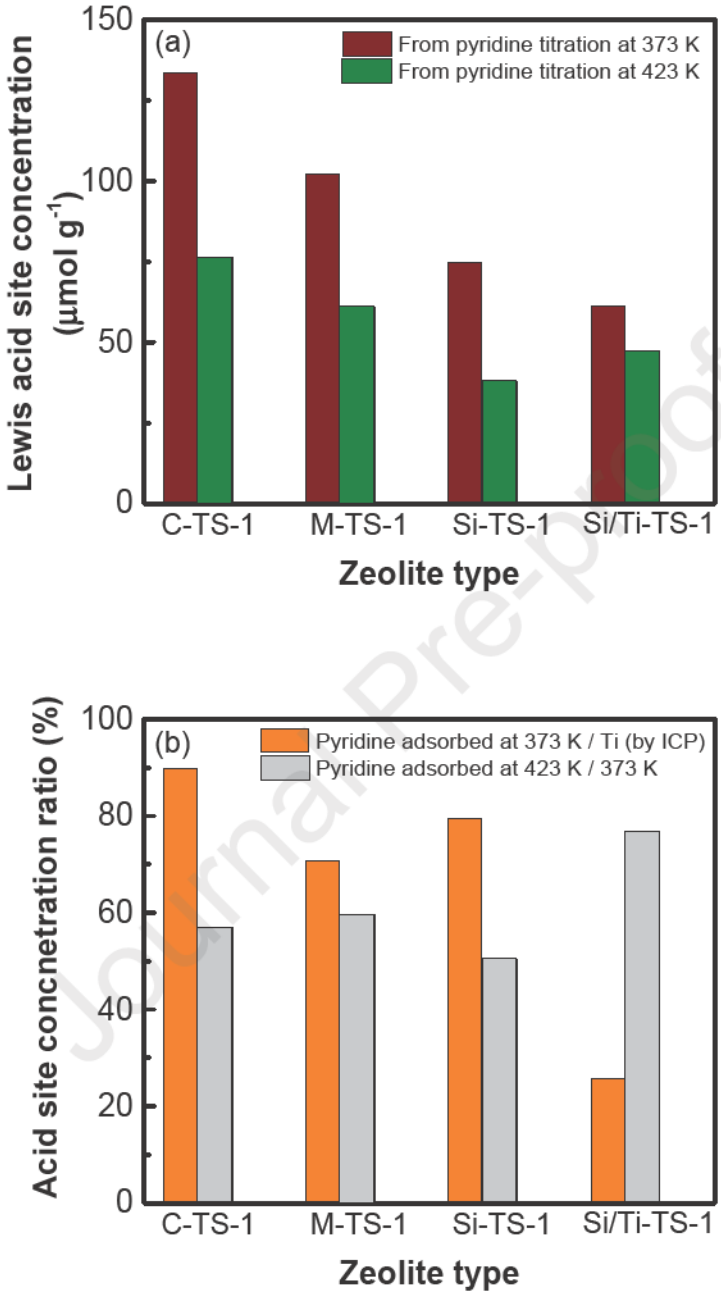

Figure 9. (a) Lewis acid site concentration determined by pyridine adsorption and (b) acid site strength indicated by ratio of pyridine adsorbed at 373 K-to-Ti concentration (determined by ICP analysis) and pyridine adsorbed at 423 K-to-that at 373 K on C-TS-1, M-TS-1, Si-TS-1 and Si/Ti-TS-1 zeolites.

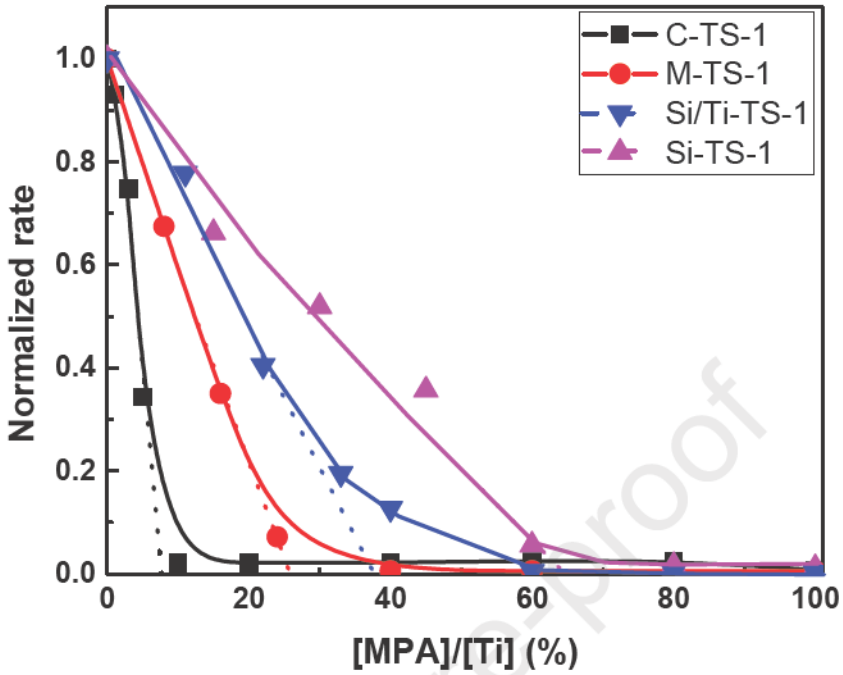

Figure 10. Normalized rate for C_8H_{14} consumption as a function of MPA-to-Ti (MPA/Ti) ratio over C-TS-1, M-TS-1, Si-TS-1 and Si/Ti-TS-1 zeolites in epoxidation of C_8H_{14} with H_2O_2. (Normalized rate is defined as turnover rate at each MPA/Ti ratio divided by that in the absence of MPA in C_8H_{14}-H_2O_2 reaction; The dashed lines represent extrapolation of experimental data to MPA/Ti (x-axis) where the normalized rate (y-axis) is set as zero in the presence of the MPA titrant.)

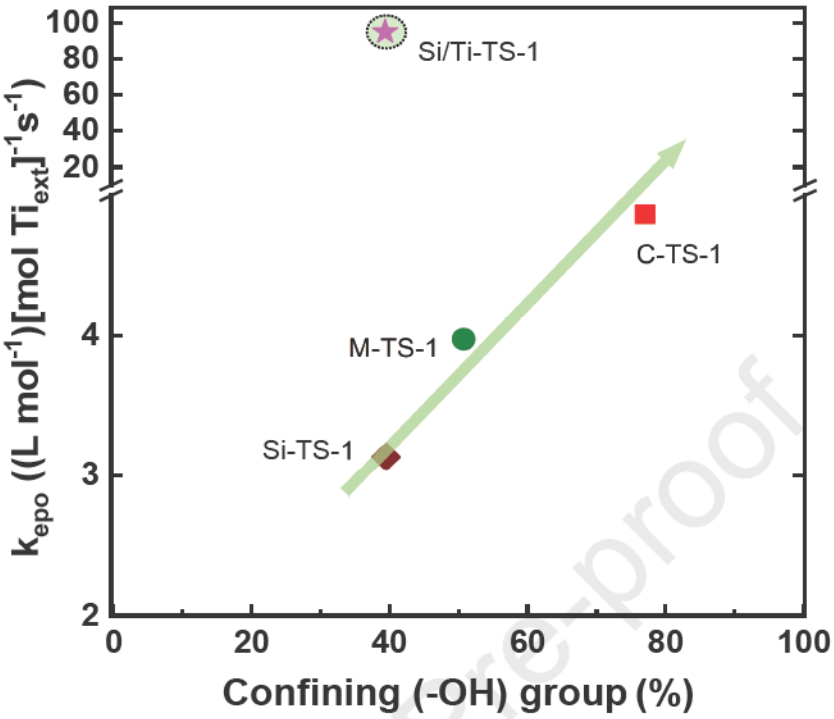

Figure 11. Rate constants of C_8H_{14} epoxidation on external active Ti-sites (i.e. Ti_{ext}-sites) versus confining (-OH) groups in C-TS-1, M-TS-1, Si-TS-1 and Si/Ti-TS-1 zeolites.

Highlights:

- External Lewis acid sites in 2D TS-1 zeolites were quantified.
- 2D TS-1 zeolites have high density of isolated surface silanol and titanol groups.
- Reactivity of external sites decreases with increasing mesoporosity in 2D TS-1.
- Decrease in reactivity of external sites is caused by loss of partial confinement.
- Kinetic decoupling of epoxidation pathways enabled catalytic behavior assessment.

Declaration of interests

☒ The authors declare that they have no known competing financial interests or personal relationships that could have appeared to influence the work reported in this paper.

☐The authors declare the following financial interests/personal relationships which may be considered as potential competing interests: